Spintronic and electronic phenomena in organic molecules measured with μSR

Ke Wang[1,2], Leander Schulz[1], Maureen Willis[1], Sijie Zhang[1], Alston J. Misquitta[2]* and Alan J. Drew[1,2]†

[1]*College of Physical Science and Technology, Sichuan University, Chengdu, 610064, P.R. China*
[2]*School of Physics and Astronomy, Queen Mary, University of London, London, E1 4NS, UK*

The use of implanted muons to probe the spin dynamics and electronic excitations in organic materials is reviewed. At first, a brief introduction to the historical context and background of the muon technique is given, followed by an outline of some of the underlying theoretical models needed to quantitatively interpret data taken on organic molecules. Caution is advised when using certain theoretical models for the interpretation of low-field spin relaxation data. The next section deals with spin dynamics in soft materials, and starts with discussing many of the key results in thin films, followed by a review of bulk measurements in three different materials classes - polymers, biologically active molecules, and small molecules. Finally, we present a detailed discussion of the density functional theory methodology when applied to μSR, and present the common issues encountered when trying to perform these calculations to support muon experiments. In particular, we discuss a method for benchmarking to manage the approximations inherent to the technique and common sources of errors that can sometimes fortuitously cancel.

1. Introduction

For several decades, muon beam techniques (known as μSR, with the SR standing for either spin rotation, spin relaxation or spin resonance, depending on the application of the technique) have become increasingly important in condensed matter research. They have been used to study superconducting,[1)] magnetic and multiferroic materials,[2,3)] spatial and temporal magnetic disorder in systems like spin glasses and liquids,[2)] spin and charge carrier dynamics in organic semiconductors,[2)] defects in conventional semiconductors,[4,5)] lithium diffusion rates in battery materials,[6)] chemical reaction rates[7)] and electron dynamics in biological molecules.[8,9)] The list is quite extensive, because of the fundamental and often unique information that μSR provides about the spin dynamics of the local environment in which the muon sits.

Despite there being some rather exotic applications of μSR, it is rather unique and sensitive spin probe that is capable of measuring local magnetic fields, whether as a result of hyperfine interactions with other spins in the muon's environment, or from some source of internal magnetism (or externally applied magnetic fields). Whilst the applicability of muon measurements on magnetic and superconducting materials is very clear (see for example refs.[1,2)]), muons can offer a significant amount of information about their local spin environment in a variety of materials that are not thought to be traditionally magnetic. This is because the muon technique is particularly sensitive to spin fluctuations, which are important in a whole host of materials, including organic molecules.[2)]

Over the years there have been many reviews and books about μSR (see e.g.[2,4,10–15)]) that describe the principles of the technique well, and there are two a special issues with many articles about the applications of μSR; one in Journal of Physics: Condensed Matter[16–36)] and another in Physica Scripta.[1,3,5–7,37–42)] We note that this article is not a comprehensive review of all papers involving muons. For completeness and convenience, however, we repeat some of this material that is relevant for the application of muons in this article.

This review is essentially split into two parts, with a focus on the spin and charge dynamics in organic molecules that can be probed with muons. The first half is an experimental section that discusses the last few decades of results. The experimental papers reviewed broadly fall into two categories - those that interpret relaxation phenomena in terms electron spin dynamics of one form or another, and those that invoke charge carrier transport models to explain the relaxation rate data. The issues with and applicability of the latter models are discussed, and put into context of conflicting evidence, such as quantum chemical calculations that demonstrate localised states. Indeed, these calculations are the subject of the second major part of this paper. In particular, they form a crucial role in understanding the μSR experiments on organic molecules, varying from a purely functional role of identifying the bonding sites of the muonium to the molecules, through to unravelling details about the electronic states that are both probed and formed. Yet, despite its importance in the field, to the best of our knowledge there is no recent review of the technique, and its pitfalls.

2. The muon technique

2.1 Background

Muons are spin $\frac{1}{2}$ leptons with a half-life τ_μ = 2.19709(5) μs, ± one electronic charge and a mass 105.65839(29) MeVc^2.[2)] It is possible to perform experiments with both negatively charged muons and positively charged anti-muons, but in this review we only consider the positively charged anti-muon, and as a result of a convention within the μSR community, refer to them as simply muons. The closest relatives of the μSR technique is nuclear magnetic resonance (NMR) and electron spin resonance (ESR). A detailed description of NMR and ESR can be found elsewhere (for example in[43)]). In general, all three techniques are complementary to each other, although all are not always applicable or useful to study a particular material.

In order to create muons, protons are accelerated by large-sale particle accelerators to several hundred MeV (for example, 590 MeV at PSI) and directed towards a light, usually

*E-mail:A.J.Misquitta@qmul.ac.uk
†E-mail: A.J.Drew@qmul.ac.uk

graphite, production target. Once the protons are within the target, they interact with other protons and neutrons to produce pions, which then decay with a half life of 26.030(23) ns[15] via the weak interaction into muons and neutrinos. Since the pion has spin zero and the neutrino spin is always opposite to the direction of its momentum, the muons produced are 100% longitudinally polarised when produced from those pions decaying at rest.

After directing to the sample, the muon's kinetic energy is reduces from ∼4 MeV to approximately 10^4 eV by inelastic scattering (with associated ionisation of the material), known as radiolysis.[44,45] The next stage of thermalisation is a continuous charge-exchange process where the muons continuously "catch" and "lose" electrons, temporally forming neutral muonium atoms. During this process the muons diminish their energy typically to a few hundred eV. Charge-exchange cycles leave a trail of electrons and cations, but unlike charges in the main radiolysis track, these are independent and separated ions and electrons, not "twinned" pairs. The final stage of the thermalisation is constituted by collisions between the muonium and atoms/molecules in the sample. In this process, the paramagnetic muonium might dissociate into a diamagnetic state, which could be, for example, an unbound bare muon, a molecule (such as MuH) or molecular ion (such as $C_2H_6Mu^+$).[2,46] The muons can stop as either species - diamagnetic or paramagnetic - and the proportion of each is very much material dependent. The situation can be somewhat more complicated than this, for example in liquids both solvated and presolvated electrons are important.[47]

Muons decay via the weak interaction into a positron, muon-antineutrino and an electron-neutrino, such that the momentum of the emitted positron is correlated to the spin of the decaying muon. Thus, by placing an array of detectors around the sample environment that are capable of detecting the positron emission direction, it is possible to track the evolution of the muon's spin as a function of time. The number of events, N, as a function of time measured with two detectors to the front (F) and back (B) of the sample is given by:

$$N_B(t) = b_B + N_B^0 \exp(-t/\tau_\mu)[1 + A_0 P(t)] \quad (1)$$

and

$$N_F(t) = b_F + N_F^0 \exp(-t/\tau_\mu)[1 - A_0 P(t)] \quad (2)$$

where $P(t)$ is the polarisation of the muon's spin, A_0 is the initial asymmetry determined by the distribution of positron energies (maximum 1/3) and is reduced by the spectrometer geometry (which is slightly different for every spectrometer), N^0 is the initial number of events recorded and b is the background emanating from cosmic muons and other sources, such as electronic noise. It is worth noting that there are different definitions of the front detector - it can be defined by the muon's momentum, or it's initial spin, and it matters not to the essential physics. In the case of vanishingly small background, the experimental asymmetry that is often plotted in publications is defined as

$$A(t) = \frac{N_B(t) - \alpha N_F(t)}{N_B(t) + \alpha N_F(t)} \quad (3)$$

where α is the detector efficiency, determined by many factors, including detector geometry, sample position, the amount of material surrounding the sample etc.

In the presence of a magnetic field B, the spins of unbound positive muons that have implanted into a sample precess at the Larmor frequency $\omega_\mu = \gamma_\mu B$, which is the vector sum of the applied field and any local field at the muon site. The muon gyromagnetic ratio is $\gamma_\mu/2\pi$=135.534(5) MHzT^{-1}. However, the characteristic frequency of the technique is different for muonium (dealt with in the next section), as several additional parameters (such as the hyperfine coupling constant with the muon and electron, the electron gyromagnetic ratio...) determine the time dependent spin polarisation of the muon.

2.2 Muonium

In the majority of molecular semiconductors, with aromatic rings and double/triple bonds, a large fraction of muons are often found in a stable bound state with an electron; the so-called muonium atom is observed. Muonium can chemically react with the molecules in the last step of the thermalisation process, joining a molecule at a site with high electron concentration, such as unsaturated bonds or aromatic rings. Fortunately, the chemistry of muonium is remarkably similar to that of hydrogen, making it a useful probe of chemical reaction rates (see refs.[47–50] for some examples, and for a recent review, please consult[51]). Moreover, when bonded to the molecule, the muonium effectively self-dopes an unpaired electron on the molecule, making it a useful probe of the dynamics of paramagnetic molecules.[2] In most organic compounds, one would expect three different species of muons in a sample: diamagnetic muons, muonium that weakly interacts with its surroundings (often referred to 'vacuum muonium') and muonium chemically bonded to a molecule (often referred to as a 'muoniated radical'). More complicated spin systems, such as a muonium atom with two electrons, have been observed in some conventional semiconductors, although to the best of our knowledge states such as these have not been observed in their organic counterparts. We will not go into the details here, but for the interested reader, we point them towards the many reviews, special issues and textbooks written over the decades of materials research with muons.[1–7,10–42,50]

In muonium, the muon and electron spins are coupled by the hyperfine (HF) interaction, which in solids has both an isotropic and anisotropic term. The value of the isotropic muon-electron HF coupling constant (HFCC) is determined by the overlap of the muon and electron wavefunctions, via the Fermi contact interaction. The muon's wavefunction is essentially a delta-function, whereas in muoniated radicals, the electron's wavefunction is spread over a large portion of the molecule. The degree of localisation of the electron's wavefunction, where it is centred with respect to the muon and the electron's orbital angular momentum determine the value of the HFCC to the muon, and this varies considerably between different muon adducts, even ones that are next to each other on the same molecule. As a consequence, the HFCC strongly varies between sites, but is readily calculable using, for example, density functional theory (DFT). This important technique is discussed in some detail in Section 5, warts and all. In addition to the isotropic hyperfine coupling constant, there

can also be an anisotropic hyperfine interaction between the muon and electron. This is averaged out to zero when the reorientation rate of the molecule is much larger than the dipolar part of the HF coupling,[50,52,53] normally the case with a liquid, but anisotropic coupling is generally present for muoniated radicals in solids.

The considerable technical details of muonium can be found elsewhere;[2] here we merely recap some of the underlying principles and important physics needed to quantitatively access spin dynamics in organic materials.

Quantum mechanically, one can consider the two-spin muon/electron system to be either as a triplet or as a singlet state. The degeneracy of the triplet states is lifted by the external magnetic field via the Zeeman interaction, which can be included in the Hamiltonian[2]

$$H_0 = -\gamma_\mu \mathbf{S}_\mu \cdot \mathbf{B} + \gamma_\mathrm{e} \mathbf{S}_\mathrm{e} \cdot \mathbf{B} + A \mathbf{S}_\mu \cdot \mathbf{S}_\mathrm{e}. \quad (4)$$

This can then be diagonalised to calculate the eigenstates of the spin system. The time evolution of the muon spin ensemble in the muonium state can be derived with the spin density matrix formalism as presented in refs[4] and,[2] where it is shown that the polarisation function consists of two parts: the non-oscillatory part, resulting in the so-called repolarisation curve, and the Rabi oscillations.

The Rabi oscillations are often very fast and are not always resolvable in experimental data. In this case, one measures the time-averaged spin polarisation of the muon ensemble. In the limit of high magnetic fields relative to the hyperfine field, the oscillation amplitude vanishes, resulting in the spins being fully repolarised. The repolarisation curve for a two-spin system calculated with some typical values of muon-electron hyperfine coupling is illustrated in Figure 1a, where it is clear from the time spectra in Figure 1b-d that even in fields as low as 1 G, the oscillations posses a low amplitude and high frequency.

The amplitude of the Rabi oscillation reduces as the applied field is increased because at high fields, the eigenstates of the spin systems are to a good approximation pure Zeeman product states. Muons implanted with their spins parallel or antiparallel to the field are thus in an eigenstate, and no time evolution of spin polarisation is expected.[55] At a particular applied field, however, cross relaxation effects cause an avoided level crossing (ALC) at what would normally be a degeneracy in the energy levels, and the eigenstates are mixtures between two Zeeman states. This results in Rabi oscillations between the levels with frequencies corresponding to the energy separation between the them. If the energy levels at the ALC correspond to different muon magnetic quantum numbers, then the time evolution induces a depolarisation of the muon (called an ALC resonance). This is shown in Figure 2a for the same coupling parameters as before (note it can be seen in Figure 1a as well), along with the time dependent polarisation in Figures 2b-g.

The isotropic HF coupling constant determines the position of the ALC and the two anisotropic hyperfine coupling constants define its width and shape. The ALC resonance shown in Figure 2a has an asymmetric shape due to the anisotropy of the HF interaction. The centre of the resonance is not exactly at the minimum of the ALC lineshape, but at a slightly higher field, as can be seen by the larger amplitude oscillations present in Figure 2e compared to the centre point in Figure 2d. The greater the difference between the two anisotropic HF coupling constants, the more pronounced the asymmetric shape of the ALC is. In addition reorientational dynamics, such as molecular rotations or vibrations, can alter the line shape due to averaging effects.[50,53]

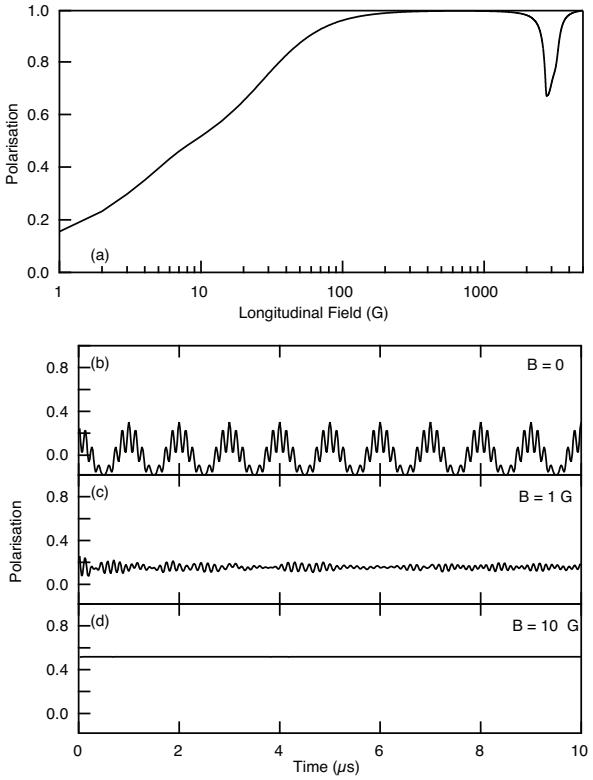

Fig. 1. (a) A time integrated repolarisation curve calculated using the Quantum programme[54] for a two spin system, for an isotropic HFCC constant of 80 MHz, and the anisotropic HFCC tensor having values of 10 and 2 MHz respectively. Time dependent polarisation for three selected fields is plotted in (b) to (d).

For a more complete description, one also must include at least one more spin in the system. The Hamiltonian in this case is more complex than for a two spin system, and a fuller description can be found elsewhere.[2] In organic materials where the muonium has bonded with the molecule to form a radical, the third spin is typically the nearest hydrogen as this would normally have the largest proton-electron HFCC, although in principle any and all nearby unpaired spins can couple. Importantly, the essential physics can be explained by considering only one additional spin, with any further spins just adding complexity. From this point forward, we simply refer to a nuclear spin as the "third" spin , although it could be any other tertiary spin (e.g a secondary unpaired electron)[42] with a finite HFCC. In taking three spins into account, we can distinguish three types of ALCs by the change of the total magnetic spin quantum number of the coupled spin system, ΔM, where $M = m_\mathrm{e} + m_\mu + m_\mathrm{k}$, and m_e and m_μ and m_k are magnetic quantum number of the the electron, muon and proton respectively. The different ALCs are:

$\Delta M = 0$: The isotropic coupling of the muonium to a nuclear spin causes a muon-nuclear spin flip-flop transition. The resonance occurs in materials with nuclear spins. It is of indirect nature, because the spin transfer from the muon

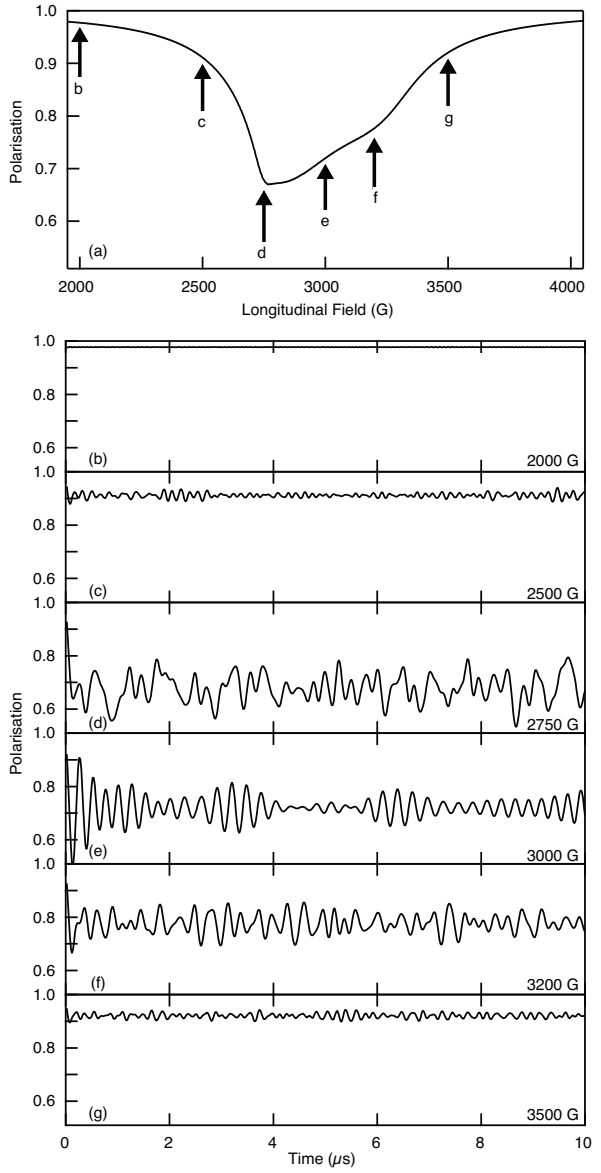

Fig. 2. (a) A time integrated ALC resonance calculated using the Quantum programme,[54] for the same values of the HFCCs as in Figure 1. The arrows indicate the fields at which the time dependent polarisation is plotted in (b) to (g).

to the nucleus is mediated by the electron. The resonance occurs at about

$$B_{\rm r}(\Delta_0) = \frac{\left|A_\mu - A_{\rm k}\right|}{2\left(\gamma_\mu - \gamma_{\rm k}\right)} - \frac{A_\mu + A_{\rm k}}{2\gamma_{\rm e}} \tag{5}$$

where effective HF coupling constants, $A_{\rm i}$ and gyromagnetic ratio γ of the three spins are signified by μ, k and e for the muon, proton and electron, respectively. These resonances are readily observed in the liquid state, and can have a FWHM as small as 2 mT, and whilst present in the solid state they can often be masked by the more intense and broader $\Delta M = 1$ resonances (see below), although $\Delta M = 0$ resonances have been observed in some of our recent experiments on the acene series and in solid-state benzene.[56] It's worth noting that there can be multiple ALC resonances for each muonium site, related to the number (and strength of interaction) of nuclear spins near the muonium site.

$\Delta M = 1$: The most simple ALC involves a pure muon-electron spin-flip arising from the dipolar components of the HF interaction. This resonance appears at the field

$$B_{\rm r}(\Delta_1) = \frac{\left|A_\mu\right|}{2\gamma_\mu} - \frac{A_\mu}{2\gamma_{\rm e}}. \tag{6}$$

It is usually only present in solid samples, because in liquids and gases the muoniated radical experiences very fast reorientations that average out the dipolar terms.[53] These resonances are often very intense and broad and can dwarf the $\Delta M = 0$ resonances in experiments.[57]

$\Delta M = 2$: These very weak ALCs, caused by the muon-nuclear spin flip-flip transitions, and they are extremely weak and are rarely observed in an experiment. They are similar to the $\Delta M = 0$ resonance but are driven by the anisotropic parts of the Hamiltonian.

ALC resonances have been shown to be a remarkably sensitive probe of dynamics in molecular systems, for example re-orientational dynamics of bucky balls[58] through to a quantitative measure of electron spin relaxation rates in organic semiconductors.[57,59–61] This latter point is one of the major subjects of this review, and so we go into the mathematics in some detail here. In order to calculate the electron spin relaxation rate from the ALC resonance, one must add the electron and mixed polarisation $\mathbf{P}_{\rm e} = \left(p_{\rm e}^{\rm x}, p_{\rm e}^{\rm y}, p_{\rm e}^{\rm z}\right)^{\rm T}$ and $p_{\rm mix}^{\rm jk}$ to the spin density matrix:

$$\rho(t) = \frac{1}{4}\left(1 + \mathbf{P}_\mu(t)\cdot\sigma + \mathbf{P}_{\rm e}(t)\cdot\tau + \sum_{\rm j,k} p_{\rm mix}^{\rm jk}\sigma^{\rm j}\tau^{\rm k}\right), \tag{7}$$

where j and k correspond to x, y, and z indicating the components of the Pauli matrices $\vec{\tau}$ and $\vec{\sigma}$ of the electron and muon. The quantum mechanical equation of motion provides a set of 15 or, if a nuclear spin is included, 63 coupled differential equations.[62,63] Assuming that the electron spins relax at a rate of $\lambda_{\rm eSR}$, the set of differential equations has to be expanded to[62]

$$\frac{{\rm d}p_{\rm e}^{\rm j}}{{\rm d}t} = \epsilon_{\rm jkl}\left[\frac{\omega_0}{2}p^{\rm kl} + \frac{\omega^*}{2}p^{\rm ml}n_{\rm k}n_{\rm m} + \omega_{\rm e}^{\rm k}p_{\rm e}^{\rm l}\right] - \lambda_{\rm eSR}p_{\rm e}^{\rm j}, \tag{8}$$

$$\begin{aligned}\frac{{\rm d}p^{\rm jk}}{{\rm d}t} = \epsilon_{\rm nlm}\Bigg(&\delta_{\rm j,m}\delta_{\rm k,n}\frac{\omega_0}{2}\left(p_\mu^{\rm l} - p_{\rm e}^{\rm l}\right)\\ &-\delta_{\rm j,n}\left[\frac{\omega^*}{2}n_{\rm m}n_{\rm k}p_\mu^{\rm l} - \omega_\mu^{\rm m}p^{\rm lk}\right]\\ &+\delta_{\rm k,n}\left[\frac{\omega^*}{2}n_{\rm j}n_{\rm l}p_{\rm e}^{\rm m} - \omega_{\rm e}^{\rm l}p^{\rm jm}\right]\Bigg) - \lambda_{\rm eSR}p^{\rm jk},\end{aligned} \tag{9}$$

which are defined by the commutators $\left[\sigma^{\rm j},\sigma^{\rm k}\right] = 2i\epsilon_{\rm jkl}\sigma^{\rm l}$ and $\left[\sigma^{\rm j}\tau^{\rm m},\sigma^{\rm k}\tau^{\rm n}\right] = 2i\left(\delta_{\rm j,k}\epsilon_{\rm mnr}\sigma^{\rm r} + \delta_{\rm m,n}\epsilon_{\rm jkl}\sigma^{\rm l}\right)$, the normal vector along the symmetry axis (axial symmetry) $\vec{n}$ and the hyperfine interaction parameters ω_0 and ω^* that depend on the host material. The indices correspond again to the coordinates x, y and z. This set of equations can generally not be solved analytically, but requires numerical simulations. The electron spin relaxation (eSR) gives rise to a damping of the Rabi oscillations and a relaxation that is superimposed on top, as shown

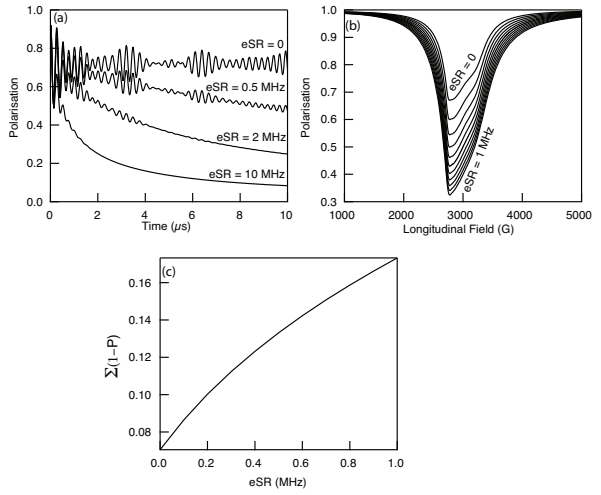

Fig. 3. (a) The polarisation as a function of eSR for 3000 G, simulated using Quantum[54] using the same parameters as in Figure 1. (b) Time integrated ALC as a function of eSR, which varies from 0 to 1 MHz in 0.1 MHz steps. (c) A plot of the sum of one minus the polarisation (shown in (c)) against eSR. After suitably scaling to the asymmetry, this is a potential method to extract the eSR without the need to explicitly model the ALC.

in Figure 3a. It is evident that this additional relaxation over time also reduces the time-averaged muon spin polarisation. In that sense, the electron spin relaxation leads to an increase of the magnitude of the ALC feature as shown in Figure 3b. Although the amplitude of the ALC increases, there are hardly any implications on the position and the width of the ALC when the electron spin relaxation rate is less than about 1 MHz. Fortunately, where this technique to access the electron spin relaxation rate is most applicable (in organic semiconductors), the values are typically lower than 1 MHz.[57,59–61] However, as the eSR increases too far beyond 1 MHz, the width of the ALC increases until eventually the amplitude of the ALC reduces,[2] taking it to the point where it is difficult to measure experimentally. In systems where there is significant disorder, such as polymers or large non-polymeric molecules, there can be a significant broadening of the ALC resonances. This often results in several resonances merging into a single line, which may have a Gaussian form. One may then try fitting of the time domain data to extract relaxation rates, rather than modelling the ALC lines, but this may require the full HFCC tensor and formation probabilities of each state, that might be impossible to obtain. However, it may also be possible to relate the area of the ALC resonance with eSR, as shown in Figure 3. In both cases, careful DFT calculations may be needed to provide estimates of the HFCCs that can then be used to calibrate the numerical method, which may take the form of calculating for individual monomer units and then scaling them all down to match the field range of the experimental ALCs (the spin density at the muon site will likely spread onto the polymer backbone, reducing the HFCC).

In the limit of small or zero dynamics, there is very little or no relaxation of the muon's spin. Models have been developed that attribute the main source of muon relaxation to intermittant HF coupling between muons bonded to the organic molecule and mobile electronic excitations. Initially, an exponential relaxation rate (see Section 3, below) was interpreted via the use of models derived for NMR in an anisotropic system with diffusive spin motion along a chain.[64,65] Interchain motion provided a cut-off to the measured relaxation rate and was included in the conventional relaxation rate theory by generalizing the motion to an anisotropic random walk on a discrete lattice.[66,67] However, it is known that the correlation function for 1D diffusion is not an exponential and hence the muon spin relaxation is not expected to be a simple exponential either. Furthermore, since the correlation time for the return to the origin of a particle diffusing in 1D is divergent, the standard NMR theory is not strictly valid, as it assumes the existence of a finite correlation time that is short compared to all other timescales in the problem. Finally, there is no explicit handing of the electron spin relaxation rate in this treatment, which will modify the relaxation rate observed. Risch and Kehr later developed a model that was intended to address some of these shortcomings. It was based on stochastic diffusion theory, with the static muon interacting through an intermittent HF coupling with an electron that is randomly diffusing along a 1D chain, and resulted in a non-exponential relaxation function.[68]

In both of the two types of analysis (exponential and the Risch-Kehr), the field dependence to the muon's relaxation rate follows a power-law behaviour if the polaron motion is mainly one dimensional. For the anisotropic motion derived from NMR theory, the correlation function for a particle revisiting the origin has a $t^{1/2}$ behaviour, so the associated spectral density derived by Fourier transformation is $f(\omega) \propto \omega^{1/2}$. This implies that the relaxation rate should follow a $B^{1/2}$ scaling law. For the Risch-Kehr model, an inverse dependence of the relaxation rate on the applied magnetic field is expected. This is often used as justification of the use of anisotropic motion models to interpret the low-field relaxation rate data (see Section 3 for a discussion and references). However, we note that all of the ways of quantitatively extracting charge carrier hopping frequencies from the muon spin relaxation have some underlying problems, discussed below.

2.3 Low-energy muon spin rotation

The previous two sections are applicable to bulk μSR, and in particular in the previous section, in extracting spin and charge dynamics in organic materials. However, spintronics applications are often found in thin film devices, and whilst bulk μSR is extremely powerful in accessing the fundamental spin physics of the materials that go into the devices, its range is too great for studying thin films. The energy of surface muons is approximately 4.1 MeV resulting in penetration depths of hundreds of μm, depending on the mass density and scattering cross section of individual atoms in the sample. For thin film samples of thicknesses of the order of tens or hundreds of nm, a much lower penetration depth is required. At the Paul-Scherrer Institute, Switzerland, a novel beamline was designed and built,[69–72] where the energy of implanted muons is adjustable in the range of 0-30 keV with a typical energy spread of 400 eV. One principle component of the beamline is a moderator where few hundred of nm thick layers of condensed inert gases such nitrogen and argon are used to decelerate the surface muons to a complete stop. This moderation process is inefficient, since only 1 muon in about 100,000 is stopped in the moderator. The muons at rest are then re-accelerated to a few keV, focused and transported to

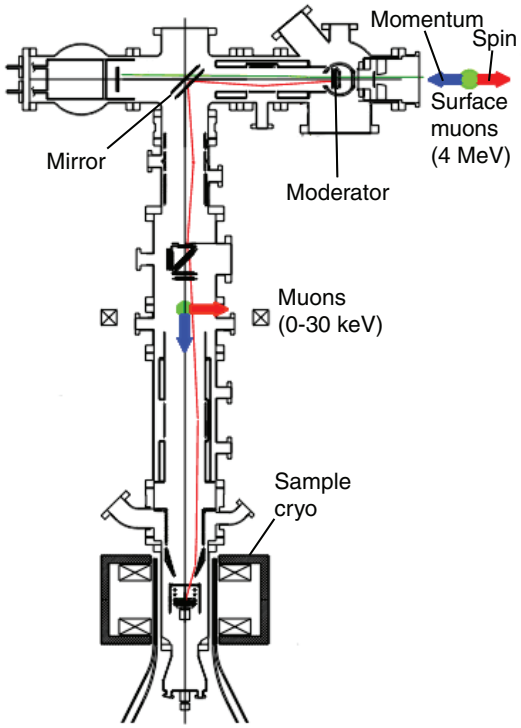

Fig. 4. (Color online) Illustration of the muon transport from the moderator to the sample of the low-energy muon spin rotation instrument at the Paul-Scherrer Institute. Adapted from.[69)]

the sample by high-voltages all the way to the sample, as illustrated in Fig. 4. The applied voltages are adjustable, enabling choice of the kinetic energy of the muons. This then allows depth resolved studies of thin films, over length scales from around ten to several hundred nm.

3. Bulk measurements of dynamics in organic molecules

3.1 Polymers

In the majority of conducting conjugated polymers, muonium is formed after muon implantation. Muonium addition to the polymer results in the formation of a negative polaron (known as a soliton) or uncharged polaron. The first μSR studies of polymers were performed on trans-polyalanine (trans-PANI), which has the rather unique property of having a ground state with degenerate bond-alternation, and as a consequence allows the formation of a free neutral polaron.[73)] A field-dependent relaxation was observed, interpreted by the presence of mobile polarons, along with a repolarisation that would be expected for localised states. In cis-polyalanine (cis-PANI), which differs from the trans-isomer in that it has no degeneracy in the bond-alternation ground state, a lower relaxation rate was observed, but similar repolarisation effect was also seen. The much smaller relaxation rate in cis-PANI was interpreted as a result of the trapped charge carrier.[73–75)] A comparison of the two can be found in Figure 5a and b. It is worth noting that original experiments[73)] were fitted to an exponential function, but it became clear later[76)] that the Risch-Kehr formalism that describes 1D stochastic motion of the charge carrier motion may be more appropriate.[68)] It was argued that the diffusion rate along the chain calculated from the RK-relaxation rate in trans-PANI shows a metallic-like behaviour at low temperatures, and above 150 K it becomes inversely proportional to the temperature, suggesting a phonon-limited metallic transport. On the other hand the interchain diffusion estimated from the cut-off fields shows an activated semiconducting behaviour, and it increases significantly above 150 K (see Figure 6 for a comparison of 300 K and 6 K). Using this logic, it was concluded that the phonons assist the interchain diffusion, while they limit the intra-chain motion.[77)]

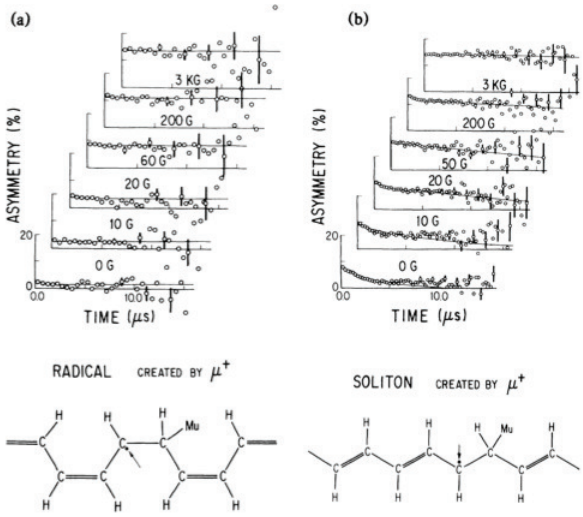

Fig. 5. Muon time spectra for (a) cis-PANI and (b) trans-PANI at room temperature for various applied longitudinal fields. The relaxation is much larger for trans-PANI than cis-PANI. The proposed pictures for the muonium states in these two isomers are also shown.[73)] Copyright 1984 American Physical Society.

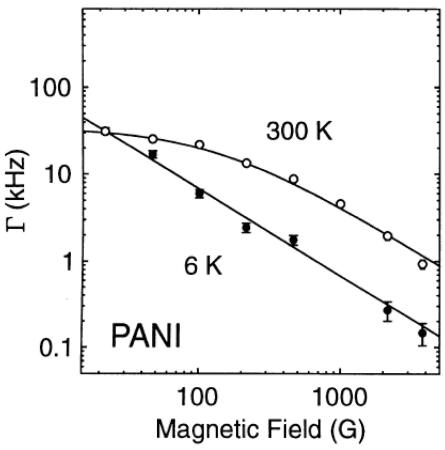

Fig. 6. (Color online) Field dependence of the RK relaxation rate in trans-PANI.[76)] Copyright 2000 Elsevier B. V.

In the majority of conducting polymers where the muonium bonds to the molecule and forms a radical, this radical cannot be an uncharged free polaron, and the simplest mobile carriers are charged solitons. A negative soliton is formed which will leave a positive charge if it diffuses away from the muon site,

so there is a binding energy to the muon site which may lead to localisation of the soliton. However, polymers (whether with a degenerate bond-alternating ground state or not) are found experimentally to have a behaviour that includes both a significant field dependent relaxation that is consistent with the mobile charge carrier models and a repolarising component of the asymmetry that is corresponds to localised electrons.[73–85] Moreover, it has been observed in recent unpublished work on P3HT (and similar polymers), a broad and intense ALC resonances[85] at high magnetic fields, commensurate with localised wave functions that are not compatible with free to diffuse charges. It has been suggested that both localised and mobile spins are present within the same sample,[86] but it is not clear what the relative importance of the localised and mobile spins are to the muon's spin relaxation. It could also be that the relaxation rate is governed by an entirely localised mechanism that results in similar field and temperature dependencies to the mobile charge carrier models. Unfortunately, DFT calculations tend to focus on smaller molecules, as not only are the polymer chains extremely long and thus the calculations would be computationally intensive, there is significant disorder in many polymers, due to different chains entangling with each other. This latter effect would result in significant disorder to local spin environment surrounding the muons, which cannot easily be calculated. There remains the option of DFT of the muoniated radical on the individual monomer block, but to the best of our knowledge this has not been extensively carried out. One further thing to note is that a repolarisation curves are notoriously difficult to interpret, and thus lead to an uncertain conclusion. One may be able to carry out careful and extensive studies of the muonium states in these materials, such as measuring ALC resonances and high TF experiments, in both liquid and solid state. We may be able to use this information, along with insight from DFT calculations, to perform modelling of various types of dynamics and try to reproduce the field dependent relaxation rates and repolarisation curves. This, however, is a major task with many unknowns, and perhaps best suited to cleaner, smaller and simpler systems.

3.2 Biological materials

In principle, it is possible to use μSR to probe biophysical systems using the same underlying analysis as the polymers. However, activity has been a little lower than elsewhere. This is likely related to two unrelated drivers. Firstly, complexity; the problems that need to be tackled in biophysics are difficult and often involve multiple steps, and the molecules are significantly more complex and larger than the polymers (which in principle have small repeat units, albeit with disorder). Secondly, there is likely some degree of self-selection - scientists using muons tend to come from a condensed matter background, and not a biological one. However, there is significant potential for expansion in this direction. For example, the HiFi spectrometer at ISIS is currently being upgraded with a laser, to allow excited states to be measured with muons, with a particular emphasis on biological systems.[42]

Analogous to the work on polymer charge carrier dynamics, muons have been used to probe electron transfer processes in a number of biologically relevant molecules, which play a central role in many biological phenomena ranging from enzymes functioning to photosynthesis. For example, μSR measurements have been performed on Cytocrome-C, a protein involved in the respiratory electron transport chain in mitochondria.[9,87,88] The relaxation of the muon's spin was observed to depend on the external field, again fitting the data using a Risch-Kehr relaxation function, and the relaxation parameter resulting from these fits is found to decrease monotonically with the applied field. Two regions with different field dependencies are observed: a weak dependence at low field and the inverse dependence expected for one-dimensional motion of the electrons in the RK model. The cut-off field is significantly reduced with decreasing temperature. The results were explained in terms of a 1D motion, with the cut-off attributed to an increase in the effective dimensionality of the motion at high temperatures due to an increased inter-chain diffusion rate.[9,87] The same method has been applied to other proteins, such as ferritin, dextran and myoglobin.[9,87,89,90]

μSR has also been used to study the molecular and electron dynamics in DNA, not only because of the role of electron transfer in the DNA damage and repair mechanisms, but also to elucidate the properties that might make this molecule a candidate for applications in nanotechnology. Electron transfer in DNA at room temperature was reported,[91] using the same models as used in polymers, with the data analysed using the RK model. An inverse field dependence of the RK relaxation parameter was observed, and the authors suggest the existence of a rapid 1D diffusion of electrons along the DNA chain.[91,92] A comparison of the results at low fields (lower than 80 G) in different DNA conformations shows a difference in the relaxation rate, which was attributed to the different arrangement of the base pairs in the DNA chain. Indeed, the authors of this study suggested that electron mobility is enhanced in the drier A-form DNA where base pairs are more densely packed, and reduced in B-form DNA where adjacent base pairs are separated further due to a higher level of hydration. At temperatures lower than 260 K, a drastic change of the muon spin relaxation rate was observed, interpreted as being due to the onset of glassy dynamics.[92] The RK relaxation function no longer reproduced the experimental data, and it was found that a Kubo-Toyabe function was more appropriate below 160 K. In fields above 1 kG the muon spin relaxation became very small and field independent. The authors interpret all of this behaviour as a suppression of the electron mobility in DNA in the glass phase.[92] It is worth noting that the conclusion regarding different mobilities in the two types of DNA is based on the assumption that the magnitude of the hyperfine fields that are fluctuating do not differ significantly between A- and B- form DNA. One would, however, expect that these fluctuating hyperfine fields differ between A- and B-form due to their different geometrical structure. It was shown theoretically that there are significant differences between the two pyrimidine bases of DNA, cytosine and thymine, which has implications on the original study.[93]

It seems clear throughout many of these studies, that it was not possible to gain a full and complete picture of the muoniated radical state prior to extracting the charge carrier dynamics, and this is a clear case where quantum chemical studies are extremely useful. It is likely that this will have an impact on the quantitative extraction of electron transfer rates, if it is even possible to measure them with muons. In most cases, other forms of dynamics - for example, spin relaxation of the

radical electron and structural dynamics of the host molecule - could be responsible for some, or all, of the muon spin relaxation reported. In this sense, due to the complexity of the materials, the study of electron transfer in biological systems is extremely challenging.

Finally, more exotic studies of biological systems have been carried out. A preliminary measurement of human hemoglobin was reported,[94] where the conclusion was that the muon is sensitive to local magnetic field and correlation time of the Fe centre in haemoglobin. The paper goes on to suggest further applications, such as in-vivo studies of brain activity, via the detection of weak magnetism in flowing blood. The authors argue that this could be achieved with future muon sources, that have a directional beam with spatial resolution of a few mm (or better), and acquisition times of a few seconds. It was noted that a source such as this are capable of scanning through any part of the brain. As a follow up, a marked difference was found in the relaxation rate between the magnetic deoxyhemoglobin compared to the non-magnetic oxyhemoglobin, and it was suggested that one application of muons is the identification of oxygenation in various regions of the brain. To the best of our knowledge, an in-vivo experiment has not been attempted.

3.3 Small molecules

Duarte and coworkers studied the muon states in zinc-phthalocyanine via TF measurements, revealing the existence of two different muoniated radical states, corresponding to the bonding of the muon at two distinct sites on the molecule[95] and a third muon addition site with significantly lower hyperfine parameters was identified later on.[96] They observed the onset of a relaxation in LF measurements from 250K, and they attributed this to the interaction with charge carriers in the LUMO.[95] Further work was analysed in accordance with the assumption that charge carriers can undergo spin exchange with the electronic spin of the muoniated radical,[97] and that the spin flip rate of this process is proportional to the carrier concentration and velocity. Using an analytical approach that takes into account the polycrystalline nature of the sample, they extract the electronic spin flip rate from the time-dependent LF-μSR measurements.[98] From these measurements, performed as a function of temperature, they also determine the activation energy for the carriers that is significantly lower than the values found from electrical measurements. They assign this discrepancy to a fast component in the conduction in the material studied.[97]

In other small molecules, such as Aluminium tris-hydroxyquinolate (Alq_3), it was found that the LF relaxation rate is consistent with the RK model, whereas it was inconsistent with an exponential relaxation.[99] As discussed above, the RK model was originally derived to interpret studies on conducting polymers that have resonance valance bonds along their backbone, and it assumes a 1D stochastic charge carrier motion.[68] By fitting the RK relaxation rate as a function of the magnetic field, it was shown that the relaxation rate exhibits the archetypical B^{-1} dependence that the RK model predicts for 1D diffusion. The authors obtain the intermolecular diffusion constant, and ultimately the electron mobility, from this field dependent relaxation rate. From the cutoff in the magnetic field dependent relaxation rate, they can also derive a limit to the interchain mobility.

The same approach is used by Saragi and coworkers[100] to investigate another organic semiconductor, 20,70-bis(N,N-diphenylamino)-2-(5-(4-tert-butylphenyl)-1,3,4-oxadiazol-2-yl)-9,9-spirobifluorene (Spiro-DPO). They observe a change in the dependence of the RK relaxation rate on the applied magnetic field as a function of temperature. In particular, as shown in Figure 7, while the data can be fitted by a power law down to low magnetic fields at low temperatures, indicating a 1D hopping of the electrons, this does not hold at room temperature. As a consequence the authors can conclude that a transition from one dimensional hopping to two or three dimensional hopping occurs in this molecule at high temperature.[100] However, as already noted, consistency with a particular relaxation function and the subsequent field dependence does not guarantee the model is correct.

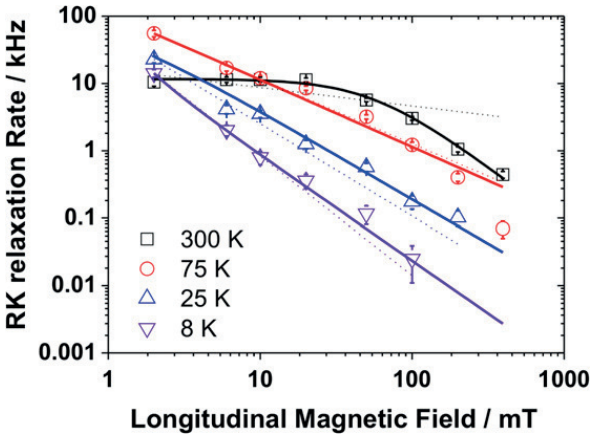

Fig. 7. RK Relaxation rate in Spiro-DPO plotted versus longitudinal magnetic field at 8, 25, 75 and 300 K. The solid lines show fits to Farazdaghi-Harris law $F(B) = A/(1 + CB^n)$, with A, C and n are constants. The dotted lines show fits to power law $F(B) = CB^n$.[100] Copyright 2013 Elsevier B. V.

Indeed, recent DFT calculations by McKenzie on the electronic state of the muoniated radicals in Alq_3 have raised questions on the validity of the RK model applied to Alq_3,[101] and this has significant implications on the applicability of the

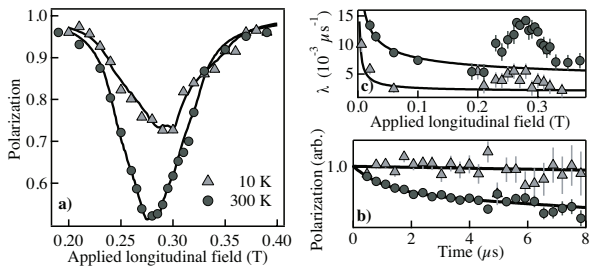

Fig. 8. Muon data for TIPS-pentacene for T = 300 K (circles) and T = 10 K (triangles). (a) The muon spin polarisation around the avoided level crossings (ALC). Modelling for these ALCs is indicated by the black lines. (b) The time-dependent muon polarisation at 0.27 T. The black lines correspond to fits to an exponential function, from which the relaxation rate shown in (c) is extracted. (c) The fitted field-dependent exponential muon spin relaxation rate showing that there is a peak in the muon spin relaxation rate around the position of the ALCs. The lines represent the expected power-law dependence for the off-resonant relaxation rate.[57] Figure 18d shows the molecular structure. Copyright 2011 American Physical Society.

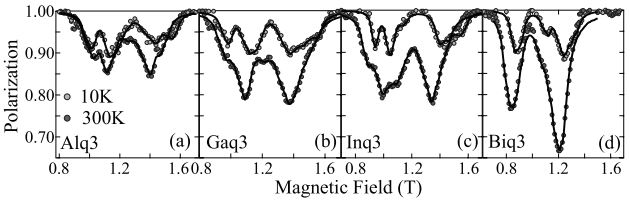

Fig. 9. Muon spin polarisation around the ALCs in the Xq_3 series, where X = Al, Ga, In, Bi: (a) Alq_3, (b) Gaq_3, (c) Inq_3, and (d) Biq_3 at 10 K (light grey) and 300 K (dark grey). Modelling for these ALCs is indicated by the black lines and is used to determine the electron spin relaxation rate, which is essentially proportional to the amplitude of the ALC curves.[60] Figure 10 shows the molecular structure of the series. Copyright 2013 American Physical Society.

model more generally. Firstly, it was shown that the energy required to transfer an electron between the muoniated radical molecule and a neighbouring molecule depends on the site of addition. Upon calculating the difference in the free energy of the initial (muoniated radical) and final (electron transferred to a neighbouring molecule) states, it was concluded that in all cases electron transfer to a neighbouring molecule is energetically unfavourable. The author then goes on to conclude that the relaxation observed in the LF-μSR spectra of Alq_3[99] are caused by some mechanism other than electron hopping, although no alternative is given. Despite this strong argument, there are some discrepancies between theory and experimental data.

The electronic state calculated by McKenzie yields the muon-electron hyperfine coupling constants, but unfortunately only two of the eight known radical states are in good agreement with experimentally derived values. The remaining six are either not predicted to be present or there are significant differences (of up to 40%) in the experimentally derived and theoretically predicted HFCCs. Furthermore, the calculations predict relatively large muon-proton coupling constants (of the order of 100 MHz for some adducts), which would result in a relatively complex set of Δ_0 ALCs, which so far have proved experimentally elusive. Unfortunately, there is no evidence of benchmarking of the DFT methodology used, and it could be that these discrepancies could be minimised if a more thorough investigation was carried out. For a more in-depth discussion on this, we refer the readers to the lengthy analysis on benchmarking found in Section 5. Nonetheless, despite these discrepancies, it is clear that the interpretation of the original experimental work on Alq_3, and other molecules that use analysis of a similar guise, needs to be revisited. Indeed, there are contradictions in the experimental data; the presence of several large-amplitude ALCs in Alq_3[60] and a clear repolarisation curve are indicative of localised electronic states, yet the effect of the electric field and the very low HFCC of 21 MHz are indicative of some form of delocalisation.[99] No such (delocalised) low HFCC states are found in other molecular species (for example, the heteroacene series,[102] the triethylsilylethynyl series,[60] the anthradithiophene series[61]).

It could be that a major component of the relaxation rate is from electron spin relaxation of the radical electron. Some decades ago, muoniated radicals were found to interact with other free radicals by Heisenberg spin exchange, which causes the electron to spin flip upon interaction with a second species. Heming et al. studied the reaction of the C_6H_6Mu radical with the stable free radical 2,2-diphenyl-1-picrylhydrazyl (DPPH) in benzene using TF-μSR and ALCs.[103] The radical lines in the TF spectra and the ALC resonances increased with increasing DPPH concentration, consistent with an electron spin relaxation picture. Indeed, more recently it has been shown that μSR and in particular ALC spectroscopy can be used to obtain a measurement of the electron spin relaxation rate of organic molecules in the solid state.[57,59,60] This use of μSR has filled in a gap, since the other experimental techniques used previously, such as magnetotransport measurements, had to rely on an under-developed and perhaps inappropriate theoretical model to extract the electron spin relaxation rate. Often, these models were initially developed for conventional band-transport materials, and it is not immediately clear if they are applicable to materials where charge carrier transport is dominated by a hopping process between discrete localised states.[104]

As discussed earlier, in organic materials where there is a high fraction of muonium, ALC resonances are observed at field values related to the hyperfine coupling constant. As has recently been shown, the change in amplitude of these ALC resonances is roughly proportional to the electron spin relaxation rate.[57,59–61] Shown in Figure 8a-d is an example of the increase in amplitude of the ALC resonance in TIPS-Pentacene, from which it was relatively straight-forward to extract the electron spin relaxation rate; indeed, the lines shown in Figure 8a are the result of the modelling, from which the electron spin relaxation rate value (0.76 MHz at room temperature) was obtained.[57] The effect of the temperature-dependent electron spin relaxation can also be observed in the time-dependent muon spin relaxation data, where the muon's spin relaxation rate becomes larger at higher temperatures (see Figure 8b and c).[57] This effect is amplified around the resonance field, where there is a significant peak in the muon spin relaxation rate as the magnetic field is scanned through the ALC, but still very much present in the off-resonance data (Figure 8b).

However prior to using this technique extensively, one must be aware that the muoniated radical sits in a different orbital to any unpaired electrons or holes in the HOMO or LUMO, and this might modify the coupling to their environment. As a consequence, it was essential to perform additional measurements that don't involve muons and quantum chemical calculations to ensure that the orbitals are not vastly dissimilar. Nuccio et al. performed time resolved photoluminescence measurements of the Xq_3 series to extract the exciton intersystem crossing rate[60] as support for the ALC measurements, shown in Figure 9. Singlet excitons that are generated by the absorption of light have a typical lifetime of ~10 ns in organic semiconductors, with the primary energy loss mechanism being fluorescence. In systems with a high intersystem crossing rate, the singlet excitons convert into long-lived triplet excitons (often with lifetimes of μs or more). These long-lived triplet excitons can then back-transfer to a singlet which results in delayed fluorescence or direct phosphorescence to the ground state, emitting a different wavelength of light. Indeed, clear phosphorescence in the Xq_3 series is readily observed as the atomic number of the central atom is increased, as demonstrated in to Figure 10a. This clearly demonstrates the impor-

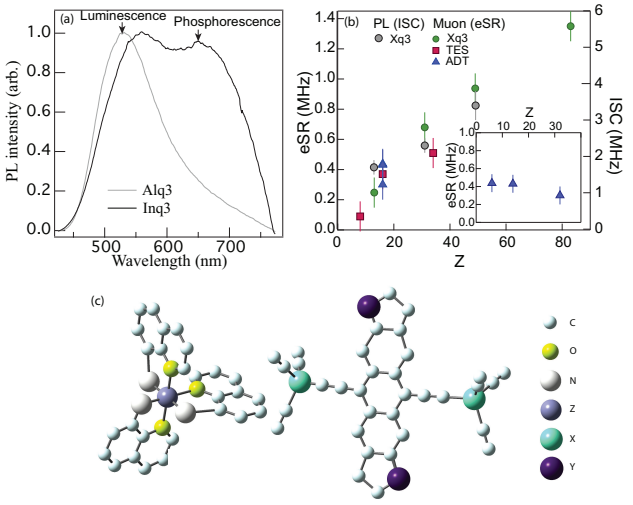

Fig. 10. (Color online) (a) The photo-generated fluorescence and phosphorescence of Alq_3 and Inq_3, which are active at different wavelengths; there would be no phosphorescence without a high interested crossing rate. (b) eSR for the Xq_3, TES and ADT series as a function of the atomic number of the substituent atom, Z. Also shown is a measure of the intersystem crossing rate (ISC) of photo-generated excitons in Xq_3, which shows the same trend and similar magnitude as the muon results. The inset shows that the ADT series is independent of mass of the substituent atom, as expected as the wave function of the muoniated electron hardly overlaps with the side groups that are substituted. Figure is adapted from[60] and also includes data from.[61] (c) The molecular structures of the Xq_3 series. The atomic substitutions were the central atom, labelled 'X', which was Al, Ga, In and Bi.[60] (d) The TES and ADT series of molecules are related. For the TES, the atoms labelled 'Z' on the side group were Si and not modified, but the two atoms on the end-rings labelled Y were substituted with O, S and Se. The formal names for these three materials are triethylsilylethynyl anthradifuran (TES-ADF), triethylsilylethynyl anthradithiophene (TES- ADT), and triethylsilylethynyl anthradiselenophene (TES- ADS), respectively. For the ADT series, the atoms on the central backbone labelled Y were S and kept constant, whereas the atoms on the side group labelled Z were substituted with C, Si and Ge. The formal names for these three materials are Tert-butyl-ethynyl anthradithiophene (TBu-ADT), Tri-methyl-silyl anthradithiophene (TMS- ADT) and tri-ethygermyl-ethynyl anthradithiophene (TGe-ADT)..[60,61] Copyright 2013 American Physical Society.

tance of the spin orbit interaction.[60] Moreover, by fitting the photoluminescence (in particular, the delayed fluorescence) to the relevant rate equations, Nuccio et al. extracted the intersystem crossing rate as a function of atomic number of the substituent atom. This is plotted in the Figure 10b, where it is clear that the same trend is observed for both the muoniated radical and the intersystem crossing rate. It is also worth noting that there is a significant change in the magnetoresistance of organic light emitting diode devices in the Xq_3 series,[105] suggesting that Spin Orbit interaction is relevant in the devices. Strengthening the case further, when substituting the side groups of the ADT series, then little effect of the substituent atom is observed.[61] DFT calculations show that this is because there is little spin density on the side groups, where the substitution happens, compared to the substitutions on the backbone of a related series of molecules.[60] It must be noted that one must be careful with the absolute values to eSR in small molecular semiconductors, as the muoniated radical electron sits in a somewhat different orbital to the free charge carriers in devices, so it is essential that quantum chemical calculations are performed to double check the relevance of the muoniated radical. However, the fact that the value of eSR extracted by muons is similar the values extracted by other techniques, and the trends are the same, clearly informs us that the technique has a lot to offer in unravelling the physics of eSR in molecular semiconductors, not least because there are few materials in this class in which measurements cannot be made.

3.4 Summary

Despite the application of charge-carrier motion models to interpret the low-field relaxation rates, we summarising by noting that all of the ways of quantitatively extracting charge carrier hopping rates have some underlying problems. To start with, assuming that it is possible for the muoniated electron to freely move, the muon spin relaxation function is a superposition of functions from all muonium states in the system, so one must have a complete understanding of all of them in order to extract hopping rates. This includes knowledge of the full muon-electron hyperfine tensor of all states (which may be transient), the proton-electron hyperfine tensor for all protons that are relevant for each muonium state, as well as other dynamics present in the system (such as a phonon mediated fluctuation of the hyperfine parameters and/or electron spin relaxation). It is not normally possible to gain this information, especially if there are delocalised states; and when it is, a large number of different experimental measurements are required, coupled with a considerable amount of modelling and DFT calculations.

One must be cautious when using the power-law field dependence of the relaxation rate to infer that charge carrier dynamics is the dominant relaxation mechanism. It is too tempting to demonstrate a match to the spectral density function of the particular type of dynamics that are expected in the sample. There could be a combination of other mechanisms that give rise to a similar field dependence of the relaxation rate that is expected from charge carrier dynamics, confusing the interpretation considerably. Moreover, the assumption of a mobile charge carrier is most likely invalid in many organic materials. Indeed, the origin of this off-resonant muon spin relaxation in organic molecules is currently unresolved, and we caution the reader about using charge carrier motion as an interpretation of their data.

Could electron spin relaxation be the major part of the muon spin relaxation rate, which was previously attributed to charge carrier dynamics[73–84,97,99,100]? Naturally, if this is the case, then the field dependence would come from the different field dependence of the various mechanisms that cause spin relaxation - for example, the hyperfine and spin orbit interactions. Depending on the energy scale of these interactions, the decoupling fields would be different, and could therefore conspire together to mimic the field dependent relaxations expected from the charge carrier motion models. Indeed, it could be that the sources of electron spin relaxation have different temperature dependencies as they could be driven by different underlying vibrations, or another mechanism all together. Moreover, the superposition of multiple muonium sites each with different exponential relaxation rates, in addition to the over-damped precession and/or relaxation from the nuclear spins interacting with the diamagnetic muons, would result in an overall non-exponential relaxation rate. And perhaps some of the more dramatic changes observed with temperature are

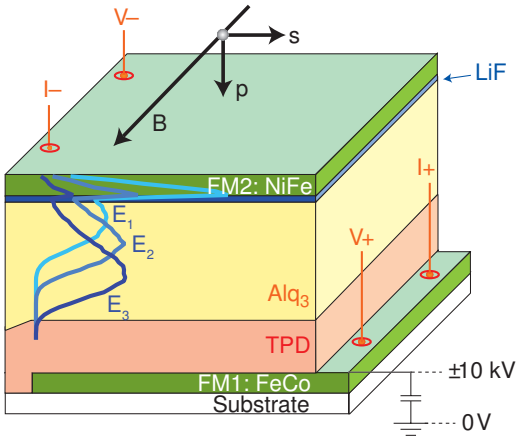

Fig. 11. (Color online) Illustration of a sample together with the experimental geometry and muon implantation profile is shown. Adapted from.[107] Copyright 2009 Nature Publishing Group.

related to structural changes driving a change in vibrational dynamics, which themselves drive electron spin relaxation. It is clear that considerably more work is needed, and indeed it is currently one of our active research areas.

4. Spintronic phenomena in thin films

4.1 Spin transport in devices measured by low energy muon spin rotation

A spin valve is a device typically composed of a non-magnetic layer sandwiched between two ferromagnetic layers, whose electrical resistance is a function of the magnetic field.[106] Most notably, the resistance is different for parallel and anti-parallel alignment of the magnetisation direction of the two ferromagnetic layers. This behaviour implies a spin transport, i.e. a spin-polarised electron and/or hole current, from one ferromagnetic electrode to the other through the non-magnetic material with complete loss of the spin information. Low-energy muon spin rotation (LE-μSR) has proven to be a very powerful technique to investigate spin transport in a fully functional organic-based spin valves.[107,108]

4.1.1 Determination of the spin coherence length

In a proof-of-principle experiment, a fully operational organic-metal hybrid spin valve, consisting from the bottom to the top of the device of a 17.5 nm thick iron cobalt layer (FeCo, 50:50 wt%), N,N-Bis(3-methylphenyl)-N,N-diphenylbenzidine (TPD) with a thickness of 50 nm, a 200 nm thick Tris(8-hydroxyquinolinato) aluminium (Alq_3) layer, followed by a 1.9 nm thin lithium fluoride (LiF) tunnel barrier and a 17.5 nm thick nickel iron (NiFe, 80:20 wt%), was investigated with LE-μSR. The active area was 18×18 mm^2 and due to the work functions of the metals NiFe was the chosen cathode. An illustration of the device is shown in Fig. 11, together with the muon stopping profiles for different implantation energies,E_{kin}, of 4.23, 6.23 and 8.87 keV respectively. The muon implantation distribution as a function of E_{kin} was calculated with TRIM.SP.[71,109] It is clear that by increasing E_{kin}, different sections of the Alq_3 layer can be probed away from the spin-injecting interface. This figure also shows the experimental geometry of the LEM measurement: the momentum of the incoming muons, p, is perpendicular to the

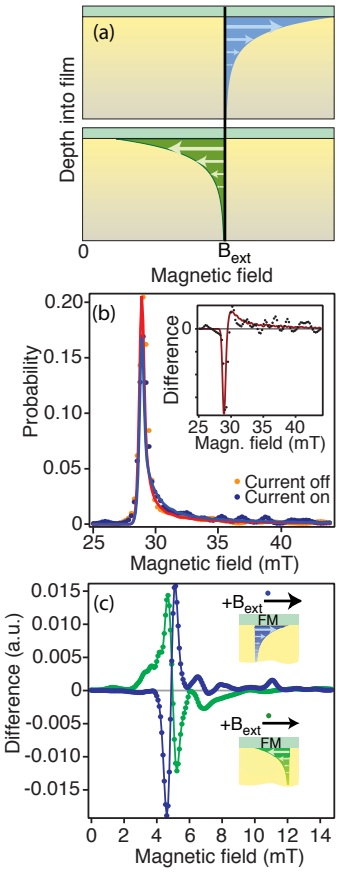

Fig. 12. (Color online) (a) The spin current can be interpreted as an additional magnetisation in the sample ("spin magnetisation"), which can contribute positively (blue) or negatively (green) to the total internal magnetisation. (b) Fourier transform of a time-resolved forward-backward asymmetry at an applied magnetic field of 29 mT, once with current on (3 mAcm^{-2}) and current off at 10 K. The solid lines are fits to skewed Lorentzians. The small difference of the internal magnetic field distribution is significant and stems from the spin magnetisation (inset). (c) The shift of weight can be observed independent of the relative alignment of magnetisation direction of the ferromagnetic layer, which defines the direction of the injected spin current, and the direction of the external field. For parallel alignment, the there is a shift towards higher fields (blue), and opposite for the anti-parallel case (green). Adapted from.[107] Copyright 2009 Nature Publishing Group.

film surface, while the muon spin, s, and the externally applied magnetic field, B, are parallel to the film plane but perpendicular to each other. The sample was mounted on a silver plate that was floated with a high voltage (several keV) as the final stage of acceleration/deceleration of the muons.

Figure 12a indicates the underlying principle behind the experiment. In the non-magnetic Alq_3 spin transport layer, the local magnetic field experienced by the muons is modified from the external field, B_{ext}, by the magnetisation as a result of the spin current. This "spin magnetisation" decreases exponentially away from the ferromagnetic-organic interface, as

$$B_{\mathrm{S}} = B_{\mathrm{S},0} \cdot \mathrm{e}^{(-z/\lambda_{\mathrm{S}})}, \tag{10}$$

where $B_{\mathrm{S},0}$, z and λ_{S} are the spin magnetisation directly at the interface, the axis normal to the sample surface and the spin coherence length of the spin current. In this figure, the filled region signifies an addition to the external field. In the lower panel, the the spin magnetisation results in a reduction of the

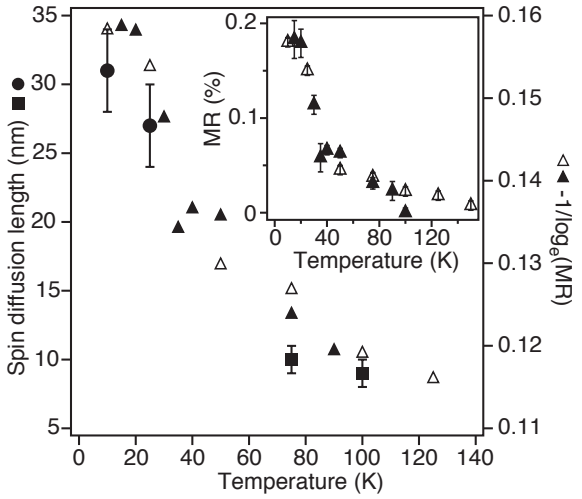

Fig. 13. Spin coherence length and magnetoresistance are strongly correlated. Figure from.[107] Copyright 2009 Nature Publishing Group.

effective magnetic field, as a result of the magnetisation of the ferromagnetic electrode being opposed to the externally applied field. Figure 12b shows the Fourier transform of the time-resolved forward-backward asymmetry, with an applied magnetic field of 29 mT where the density of the injected current was either zero (OFF) or set to a value of 3 mA·cm^{-2} (ON). The comparison of the "ON" and "OFF" data reveals a relatively small but significant difference, best observed in the inset, which shows the difference between the two states. The magnetic field distribution for the ON case is slightly shifted to higher values of the magnetic field. This is exactly the effect that is expected if the effective magnetic field is increased due to presence of the current-induced injection of spin-polarised charge carriers, and can be thought of as a change in the skewness in the field distribution. To ensure that the effect observed was truly related to the injected spin polarisation, data was taken where the magnetic layer had parallel or antiparallel magnetisation in relation to the applied magnetic field. In the case of anti-parallel magnetisation, the change in skewness would be negative, whereas in the parallel configuration, the change of skewness is positive. This is shown in Figure 12c, confirming that the effect is spin polarised. It is intuitively clear that the depth-dependent data contains information about the spin diffusion length in the non-magnetic layer, which can be extracted from the time-domain data directly. The Fourier transforms shown in Figure 12 indicate that the field distribution that the muons observe is a skewed Lorentzian. although there are actually two components to the data. There is a component with a small relaxation rate, from the muons that stop in a non-active part. For example, in the gold (or aluminium) contacts, in the silver sample holder etc. In this case, the precession of the muon spins is only driven by the external field, B_{ext}. The second component corresponds to those muons whose spin relaxes more strongly, as a result of the dipolar fields inside the sample and the spin current, when present, which result in a depth dependent internal field, $B(z)$. This signal mainly stems from the muons which are implanted into the active part of the spin-valve device. There is also a third component, from the muons that thermalise as muonium, manifesting itself as a "missing" or "invisible" fraction, invisible by virtue of the high frequencies that the spins of these muons are precessing at.

When the spin current is off, the only resulting internal field that the muon experiences is governed by the dipolar field distribution. The parameters describing this are then kept constant when analysing the ON state. The ON state was then fitted to Equation 10 with appropriate weighting for the stopping profile of the muons, at 10 K, 25 K, 70 K and 90 K, to extract the spin diffusion length. This is shown in Figure 13, plotted together with the macroscopic magnetoresistance (MR) measured independently. The MR had to be measured on two other samples with the same nominal composition. It is evident that both quantities follow a similar trend. This suggests that the spin diffusion length is, among others, a key player for the MR in an organic-metal hybrid spin valve device. Because μSR measures homogeneously over the entire area of the device, the spin is injected across the whole ferromagnetic metal - organic interface, not through structural deficiencies in the thin film such as pinholes.

Finally, it was noted that the field distribution in Figure 12 has a skewed Lorentzian, and that a change in skewness of the distribution is a measure of the sign of spin polarisation with respect to the magnetisation of the closest electrode. This was used in a follow-up paper, discussed below, to understand the role of various interfaces on spin propagation between the electrode and organic semiconductor.

4.1.2 Engineering spintronic interfaces

In a follow-up experiment, the manipulation of the spintronic properties of metal-organic spin valves were investigated by comparing two nominally identical samples except for an interlayer at the spin-injecting metal-organic interface.[108] One sample consisted of iron cobalt (50:50) as bottom layer, a lithium fluoride (LiF) layer, an organic spacer layer and a nickel iron (80:20) top electrode. The composition and the thicknesses of the thin film device from the top to the bottom can be summarised as NiFe 20 nm / LiF 1 nm / Alq_3 150 nm / FeCo 17 nm. The second sample had the same composition but without LiF layer: NiFe 20 nm / Alq_3 150 nm / FeCo 17 nm. The active area was for both samples about 16 $\times$ 16 mm^2. The removal of the very thin LiF layer has practically no effect on the implantation profile of the muon because LiF is thin and only has a low mass density. In all cases and both samples, the magnetisation of the ferromagnetic layers was oriented parallel to the external magnetic field.

To determine the impact of the polar LiF layer, two independent and fundamentally very different experiments were performed. The first one is a classical macroscopic magneto-transport measurement at 20 K and an applied voltage of 20 mV. Figs. 14a) and d) show the magnetoresistance of both devices, once with LiF and once without. It is immediately clear that removing the LiF layer reverses the magnetoresistance of the device. In a second experiment, LE-μSR was employed to measure the behaviour of the "spin magnetisation" described above. The change of skewness of the Lorentzian, $\Delta = \Delta_V - \Delta_{V=0}$, is plotted in Figs. 14b and e, measured at 10 K for two implantation energies at various voltages. This skewness change represents the injected, or extracted, spin polar-

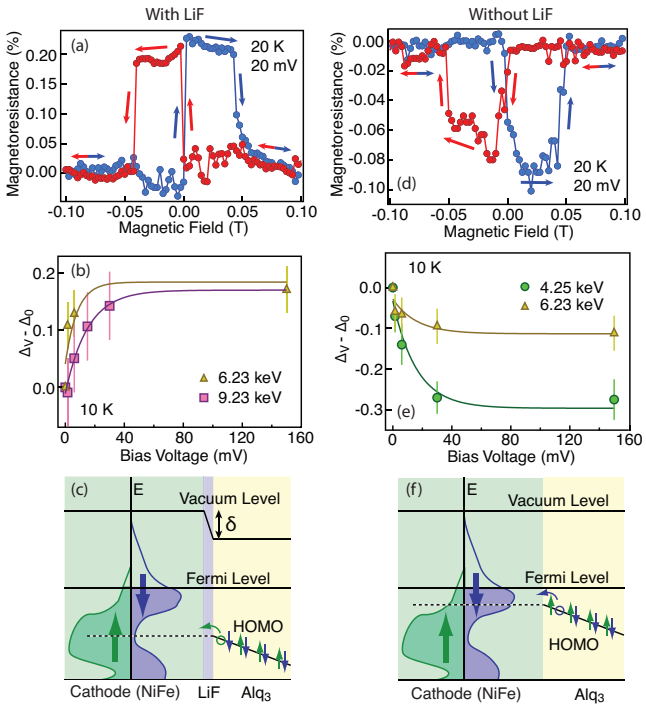

Fig. 14. (Color online) Results of nominally identical samples, except for a lithium fluoride (LiF) polar layer, are compared. (a), (d): The macroscopic magnetoresistive measurement has a different sign. LiF can modify the spintronic property of a device to the extent that it reverses. (b), (e): Microscopic μSR measurements: The change of the skewness, similar to the change of the skewness shown in Figs. 12b and c, also has a different sign depending on the usage of the LiF. Measurements were performed at B_{ext} = 27 mT at T = 10 K. (c), (f): The reversal of the spintronic property can be understood by a vacuum level shift and an accompanied different energy alignment at the metal-organic interface. Different regions of the density of states of the spin sub-bands re now accessed (see text). Adapted from.[108] Copyright 2011 Nature Publishing Group.

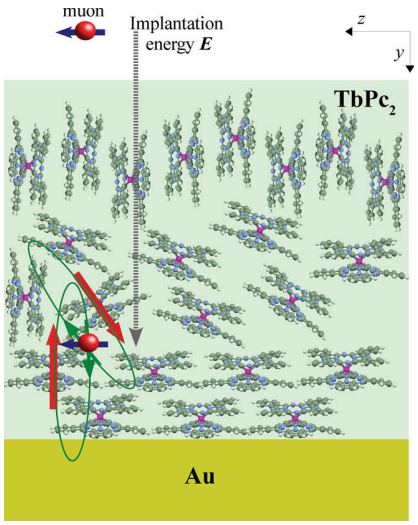

Fig. 15. (Color online) Experimental setup of the LE-μSR measurements of the spin dynamics of $TbPc_2$ near a substrate. Figure from.[115] Copyright 2012 American Chemical Society.

isation. The first significant difference is that the change is positive with LiF and negative without. This result is qualitatively in full agreement with the change of the sign of the magnetoresistance. It is worth mentioning that the saturation of the skewness change is also in agreement with reduction of the magneto-resistance as a function of increasing voltage observed by (almost) every other research group:[106,110–112] A high voltage facilitates the injection of both spin species with similar probability, thereby reducing the magnetoresistance.

To explain these findings it is important to understand that the muons measure a higher local magnetic field, B_S, which is formed by the injected spin majority electrons (or extracted spin majority holes). A reduced skewness originates from the decreased magnetic field stemming from the higher number of spin minority charge carriers. Due to the closeness of the HOMO level of Alq_3 and the work function (Fermi level) of the NiFe electrode, the current is dominated by spin majority holes that are extracted from the HOMO into the spin majority band of the ferromagnetic electrode, also because of a low switch-on voltage of about 30 mV. LiF has strong electric dipole moments which can induce a vacuum level shift of up to 1 eV.[113,114] A shift of the vacuum level in Alq_3 is accompanied by a shift of the HOMO level. The energy levels of the organic semiconductor align with a different energy regime of the ferromagnetic metal, thereby shifting the dominance from one spin-dependent subband to the other one as illustrated in Figs. 14c and f. Holes can be extracted (well) below the Fermi level, in contrast to electrons where this is not possible since there are no vacancies. Since the spin-dependent density of states is now different at the new energy level, the spin polarisation of the extracted holes has reversed.

This important result opens the door to new investigations where so-called spinterface (spin-interface) manipulations significantly impact on the spintrontric properties of metal-organic hybrid spin valve structures.

4.2 Spin dynamics in thin films of single molecular magnets

The single molecular magnet (SMM) terbium(III) bis(phthalocyanine) ($TbPc_2$) is recently attracted the interest of many researchers due its stability if evaporated (usually SMM decompose if evaporated). This opens the door to investigate their potential use on in spintronics devices, which requires the ability to process and deposit the material on substrates. The magnetic interactions in the SMM, however, can change in the vicinity of the substrates.[115,116] Hofmann et al. investigated $TbPc_2$ in form of a (1) bulk powder, (2) 1 μm thick and (3) 100 nm thin layer on top 200 nm polycrystalline gold deposited on freshly cleaved Muscovite mica substrates. These samples were probed with zero-field low-energy muons similar to the illustration in Fig. 15. A typical data set as measured (except for the normalization) is shown in Fig. 16a). The muons are implanted perpendicular to the surface. Upon interaction with the local field, their spin direction is altered. The change of the spin direction can be traced as a function of time and provides information about the probed local field and the surrounding magnetic moments. There are two contributions to the local magnetic field experiences by the implanted muons, a static and dynamic component, the former is represented by a fluctuation rate, ν, and the latter by the width of the static magnetic field, δ. The data was fitted with a so-called Lorentzian-type

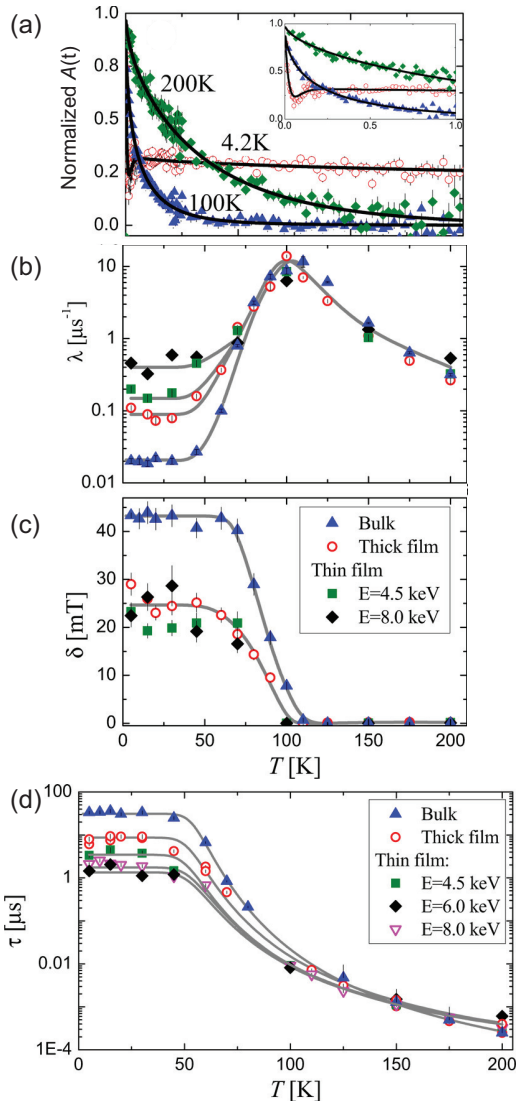

Fig. 16. (Color online) (a)Normalized forward-backward asymmetry of bulk $TbPc_2$ measured with zero-field LE-μSR. Inset: Same as main graph but shorter time axis to emphasis minimum at low temperatures. (b) Characteristic timescale of relaxation of the signal, λ. Underlying function is a square root exponential. (c) Width of the static field distribution, δ, experienced by the muons. (b), (c) Solid lines are a guide to the eye. d) Correlation time of the local magnetic field from the SMMs experienced by the muons, τ. Solid lines are a fit to Equ. 12. Figures are adapted from.[115] Copyright 2012 American Chemical Society.

Kubo-Toyabe to account for the static part combined with a square-root exponential, determined by the parameter γ, which contains information about the dynamics of the local field. The forward-backward asymmetry can be written as

$$A(t) = \frac{A_0}{3}\left[1 + 2(1-\gamma\delta t)\mathrm{e}^{-\gamma\delta t}\right]\mathrm{e}^{-\sqrt{\lambda t}}, \qquad (11)$$

where A_0 and λ are the initial forward-backward asymmetry and the gyromagnetic ratio of a muon. The parameters δ and λ for all three samples are shown in Fig. 16b and c. The similarity of the behaviour of all parameters implies that the qualitative nature of the magnetic properties of the SMMs does nothing when one reduced the thickness from bulk to at least 100 nm. At low temperatures, the dynamic part can be described by $\lambda = 2\tau/3$ whereas at high temperatures the data

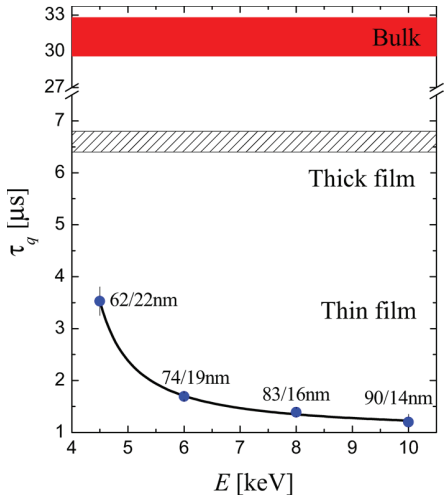

Fig. 17. (Color online) Phenomenological correlation time, τ, representing quantum tunnelling between $J_z = 6$ states as a function of the $TbPc_2$ thickness. The numbers adjacent to each point correspond to the mean/rms depth of muons, respectively. Figure from.[115] Copyright 2012 American Chemical Society.

can be correlated to τ with $\lambda = 2\tau(\delta_0\gamma)^2$, where δ_0 is the size of the fluctuating magnetic field at the measured temperature and can be determined with $\delta_0 \approx \delta(T \to 0)$ (dipolar magnetic moment of a single $TbPc_2$ molecule). The obtained correlation time is plotted in Fig. 16d).

The correlation time, τ, originating from the surrounding SMMs with respect to the location of the muon, can be related to two factors: a phonon-induced transition between two magnetic states of a molecule (between $J_z = 6$ and 5), described by τ_{sp}, and a phenomenological constant contribution to represent quantum tunnelling, τ_q. Thus,

$$\frac{1}{\tau} = \frac{1}{\tau_{sp}} + \frac{1}{\tau_q} \qquad (12)$$

This equation together with $1/\tau_{sp} = \Delta^3 C \exp(\Delta/T)$, where Δ and C are parameter that describe the spin-phonon interaction and the energy gap between the spin states. Using this model to fit the μSR data provides concrete values for τ_q as shown in Fig. 17. In addition, τ_q is 31.2±1.6 μs for bulk $TbPc_2$ and 6.6±0.2 μs for the 1 μm film. Hence, the quantum tunnelling correlation time between a SMM moment and its environment can alter from the bulk value down to about 1.4±0.1 μs for 14 nm thin films, i.e. very close to the Au substrate. This means that the spin dynamics is strongly enhanced close to the Au substrates. However, it is further argued that a direct interaction (via exchange interaction or similar) between substrate and $TbPc_2$ is not very likely. The authors suggests that a depth-dependent packing of the $TbPc_2$ molecules may be responsible for a modified super-exchange mechanism between neighbouring $TbPc_2$ molecules. Different packing implies a controlled modification of the spintronic properties by, for example, simply using different deposition methods.

5. Density Functional Theory (DFT)

5.1 Introduction to DFT-based methods

From the discussions in the previous sections, we know that quantum chemical calculations of the wavefunctions of the

muoniated radicals are extremely important when performing a quantitative analysis of μSR spectra. Indeed, it is our experience that in most experiments, DFT calculations are an essential first step that is needed prior to performing an experiment. This is because searching for ALC resonances experimentally can take a considerable amount of time, and DFT calculations can considerably reduce the time needed to find them. Moreover, these calculations can be used to perform a qualitative, and sometimes quantitative interpretation of the data. Because of the importance of DFT in this respect, we will discuss the DFT method applied to μSR in some detail. This is of particular importance, as to the best of our knowledge, there has not been any recent review of DFT applied to μSR. To discuss the essential issues, we limit ourselves to calculations of isotropic HFCC for the muon and proton, that are most appropriate for liquid state muon experiments. In particular, we discuss the issues around accuracy of calculated HFCC, what is needed to improve it, and the benchmarking that is necessary to undertake for each system studied.

In most μSR experiments, the assignment of the sites to which the muons are bonded cannot be achieved without theoretical calculations of the hyperfine structures of both the muon and the proton, that together determine the ALC spectral lines. The hyperfine structure is especially sensitive to electron correlation: consider that at the Hartree–Fock level of theory, where no correlation is present, the isotropic HFCCs often differ from their experimental values by as much as 100%.[117] Kohn–Sham (KS) DFT provides a means of including the effects of electron correlation potential, while retaining a low computational cost. KS DFT has been shown to exhibit a reasonably good accuracy in calculating the electronic structure of systems of many atoms,[118] and has been used to reproduce reasonably good results of HFCCs.[119–121] This theory is therefore in common use for calculations of HFCCs in most μSR experiments. However, despite the accuracy of DFT, in some situations DFT does not perform well or may be ambiguous for the following reasons (see Ref.[122] for an overview and references):

- The first problem — one that affects all first principles calculations of the HFCCs — is the rather high sensitivity of the isotropic HFCC to the basis-set. This problem is a consequence of the local nature of the isotropic hyperfine interaction and it may be overcome, at least in principle, by employing basis sets with heavily contracted s orbitals,[123] or by expanding the size of the basis-sets.[124] Alternatively, we may circumvent the locality of the HFCC by applying alternative Fermi-contact operators that globally sample the wavefunction.[125–130]
- For small systems KS DFT does indeed appear to result in fairly accurate isotropic HFCCs,[119–121] but as we shall see below, this good performance does not carry on to larger, more delocalised systems. Here the local and semi-local exchange-correlation functionals exhibit a self-interaction error[131] that results in an excessive delocalisation of the electronic density. This error may be reduced by increasing the amount of exact, or Hartree–Fock-type exchange in the functionals, as is done in hybrid and range-separated functionals. However, as we shall demonstrate, this improvement in the functionals may worsen the agreement with experiment.

In addition to the above concerns, the accuracy of DFT-based HFCC calculations relies on the molecular geometry used. This is especially true for solid state radicals, where the nuclear configuration is significantly affected by the crystalline environment.[57] However, since the ALC resonances in the solid state are usually $\Delta M = 1$ resonances, that is, they are functions solely of the muon HFCCs, the assignment of the sites to which muonium is bonded is easier than in liquid state, where only $\Delta M = 0$ resonances are present, and these depend on both the muon and proton isotropic HFCCs.

Moreover, though the muon may, for practical purposes, be treated as if it were an isotope of the proton, in contrast to the proton its small mass means anharmonic vibrations will effect the muon more. Consequently, one would expect the spin density at the muon measured by μSR to deviate from that of the equivalent proton in the protonated radicals measured by ESR techniques.[132] Therefore the zero point energy (ZPE) corrections, including both harmonic and anharmonic vibrational effects, may be expected to be essential in the calculation of the HFCCs for the muon, and even the proton. However, this comes at an additional, and often significant computational cost.

For calculations in crystalline systems, the geometry optimisation of the unit cell can be carried out using semi-empirical methods such as PM3,[133] which empirically addresses the light isotope effect of the muon and includes effects of the crystalline packing. Subsequently, the HFCCs may be calculated using DFT[134] in this hybrid, PM3/DFT approach. The HFCCs are sensitive to the optimised crystalline structure, which is the most challenging to deal with, especially as Mu has a larger isotope effect than, say, deuterium. PM3 provides a qualitatively reasonable basis for interpreting the isotope effect on the electron affinities of the fully or partially deuteriated pyrene and benzene (and the anion radicals),[135,136] and has also been shown to be accurate enough to calculate the crystal structures of several organic compounds.[137–139] It has also been used in combination with unrestricted Hartree–Fock (UHF) to evaluate the spin densities, and this method, PM3/UHF, has been used to study the distributions of the spin densities for some of the organic radical crystals.[140,141] As explained above, DFT may be a better approach to studying the spin densities, so we expect the PM3/DFT hybrid method to provide a good compromise between accuracy and computational efficiency, particularly for studies on large systems, such as those consisting of polymers.[134]

For other moderately large organic systems, muon HFCC calculations for solid state radicals may in practice be performed without taking into account the effects of the crystalline environment.[142] Specifically, the geometry optimisation and calculation of HFCC has been done under the circumstance that the system is taken as a free molecule, subsequently the isotope effect of Mu is simply addressed by the multiplication of a factor 1.2.[142]

Calculations on gas or liquid phase radicals require a high accuracy for both muon and proton isotropic HFCCs, which together determine the ALC resonance, and are therefore more sophisticated. For the sake of the well characterised HFCCs by both EPR and μSR experiments, the data of muo-

niated and pronated benzene (C_6H_6Mu and C_6H_7, known as Muonium-substituted cyclohexadienyl and cyclohexadienyl, respectively)[132] can be used as a benchmark for the quality of DFT calculation. In order to take into account the isotope effect of Mu, a diatomic Morse potential was used firstly for C–H and C–Mu, and an 4.9% increase of the averaged bond lengths for C–Mu, and then the reduction in the methylene C–H bond in the C_6H_6Mu was achieved by the re-optimisation of the structure with the C-Mu bond length fixed at a value which is by 4.9% greater.[143,144] Later on the calculation regarding the anharmonicity of the C_6H_6Mu was performed by Probert et al.[145] using the spin polarised Projector Augmented Wave (PAW) technique based on DFT. Geometry optimisation was performed on a C_6H_6Mu with a Mu molecule in a finite box, and the C-Mu bond-stretching vibrations was calculated by displacing the Mu from its equilibrium position in the bond direction and then simulating the undamped dynamics of the system. They believed the dynamical approach to be significantly more accurate than extracting a vibrational frequency by fitting to some potential energy surface or using a semi-empirical technique, as the amplitude of zero-point vibration is large because of the very low mass of the Mu. Hudson et al.[146] proceeded another method by calculating the HFCC at the vibrational average over the stretching, in-plane and out-plane mode with Mu, assuming that the muon is an light atom, and their final conclusion was that the stretching mode provide absolutely the predominant contribution.

Moreover, due to the importance of solvent effects in the calculations of hyperfine structures of the organic radicals,[147] the investigations of the subtle solvent effect on the isotropic HFCC for C_6H_7 or C_6H_6Mu in water, were done both implicitly and explicitly- the former overestimates the effect while the latter reduces the overestimation slightly, and their conclusion was that the increase in the muon HFCC is mainly due to an increased polarisation of the singly occupied molecular orbital (SOMO) towards one side.[148]

For other small muoniated radicals and systems that are less rigid (for example, having a torsional degree of freedom) the conformational averaging and ZPE vibrational averaging are usually taken at a reasonable computational expense. There are quite a few articles that describe the various methodologies.[149–152] However, much attention has been drawn onto the muoniated aromatic molecules (such as acenes) due to the simplicity in the systematic extension of their chemical structures. They are relatively conformationally rigid so that the uncertainties in the DFT calculations are largely reduced. Therefore, in this section, we will also take a look at the calculations of the gas or liquid phase of those radicals (all shown in Figure 18) as examples of the methodologies that we will introduced below.

5.2 Theoretical background

The HFCCs of the muon and the protons can be evaluated from electronic structure calculations and the nuclear dynamics of the system of interest. However, as the isotropic HFCC depends on the spin-density at a single point, this quantity is exceptionally sensitive to the choice of density functional, the basis set used, the functional form of the Fermi-contact operator, and, additionally, to the nuclear motion, which may be treated at either the harmonic or anharmonic level of theory. These factors make the calculation of the isotropic hyperfine tensor a challenge, and we will explore some of these issues below.

5.2.1 Hyperfine tensor

The hyperfine coupling between electronic spin $\mathbf{S}_e$ and the spin of the nucleus N or muon ($\mathbf{S}_N$ or $\mathbf{S}_\mu$), can be described by the hyperfine Hamiltonian which is the third term in equation (4):

$$\hat{H}_0 = \mathbf{S}_e^T \cdot \tilde{A} \cdot \mathbf{S}_\mu \tag{13}$$

where $\tilde{A}$ is the hyperfine coupling tensor which consists of an isotropic part (A_{iso}) and an anisotropic part ($A_{\text{aniso},ij}$) as follows:[153]

$$A_{ij} = A_{\text{iso}}\delta_{ij} + A_{\text{aniso},ij}. \tag{14}$$

In a radical with one unpaired electron, A_{iso} is proportional to the spin density ρ_s at the nucleus N:

$$A_{\text{iso}} = \frac{8\pi}{3}\gamma_e\gamma_I\rho_s(\mathbf{R}_N), \tag{15}$$

where γ_e and γ_I are the gyromagnetic ratios of free electron and the nucleus N, $\mathbf{R}_N$ is the position of the nucleus N, and $\rho_s(\mathbf{r})$ is the electronic spin density at the position $\mathbf{r}$. A_{iso}, which is also called Fermi-contact coupling constant, originates from the hyperfine interaction between the nucleus and the s-electron at the nuclear site.[154] Expressed in terms of the single electron spin orbitals $\{\psi_p\}$, A_{iso} may be expressed as:[155]

$$A_{\text{iso}} = \frac{8\pi}{3}\gamma_e\gamma_I \sum_{p,q}\langle\psi_p|2\hat{S}_z\delta(\mathbf{r}-\mathbf{R}_N)|\psi_q\rangle\, D_{pq}, \tag{16}$$

where D_{pq} is the density matrix and $\hat{S}_z$ is the z-component of the electronic spin operator. Here $\delta(\mathbf{r})$ is the delta-function operator which indicates that the isotropic HFCC only depends on the spin-density at one point, i.e. at the nucleus.

Within the unrestricted open-shell framework, the spin density at the nucleus will arise from the SOMO and the spin polarization in the doubly occupied molecular orbitals (DOMOs) and may thus be written as:

$$\rho_s(\mathbf{R}_N) = \rho_s^{\text{SOMO}}(\mathbf{R}_N) + \rho_s^{\text{SP}}(\mathbf{R}_N), \tag{17}$$

where, if the electron in the SOMO has spin α, $\rho_s^{\text{SOMO}} = \rho_\alpha^{\text{SOMO}}$ and the spin polarization contribution is $\rho_s^{\text{SP}} = \rho_\alpha^{\text{DOMO}} - \rho_\beta^{\text{DOMO}}$. In the restricted open-shell framework, the latter contribution is zero.

Correspondingly, the anisotropic component of the hyperfine coupling tensor, $A_{\text{aniso},ij}$, may be expressed in Cartesian form as:[122,155]

$$A_{\text{aniso},ij} = \gamma_e\gamma_I \sum_{p.q}\langle\psi_p|2\hat{S}_z\left(\frac{r_N^2\delta_{ij} - 3r_{N,i}r_{N,j}}{r_N^5}\right)|\psi_q\rangle\, D_{pq} \tag{18}$$

where the $\mathbf{r}_N = \mathbf{r} - \mathbf{R}_N$ and i and j label the Cartesian components of this vector.

Alternatively, the hyperfine tensor $\tilde{A}$ may be defined in terms of its principle values A_x, A_y, and A_z, from which the isotropic HFCC term, A (which is the same as A_{iso}), and two anisotropy terms D and η may be defined. The anisotropy term D describes the axial asymmetry of system, and the rhombic component η describes the departure from axial asymmetry. The relationship between A/D/η and $A_x/A_y/A_z$ is as follows: $A_x = A - D/2 + \eta/2$, $A_y = A - D/2 - \eta/2$ and $A_z = A + D$.[156]

Consequently, $A_{\rm iso} \equiv A = (A_x + A_y + A_z)/3$. In general the isotropic HFCC, A, describes the spin density at the various nuclei in a molecule, while the anisotropic HFCC terms, D and η, reflect the asymmetry of the spin density distribution about the nucleus.

5.2.2 Basis-sets

The basis set refers to the set of linearly combined one-electron wave functions that are used to build up the molecular orbitals. Both the Gaussian-type orbital (GTO) and the Slater-type orbital (STO) are the atom-centered basis-sets that are most commonly employed. A contracted primitive Cartesian GTO is defined as:[157)]

$$\phi_{pqr}^{\rm GTO}(x,y,z) = N \sum_{i=1}^{n} c_i (x-R_x)^p (y-R_y)^q (z-R_z)^r \exp(-\zeta_i(\mathbf{r}-\mathbf{R})^2) \tag{19}$$

where the $\{\zeta_i\}$ are the exponents of the basis functions in the contraction, the $\{c_i\}$ are the contraction coefficients, and $\mathbf{R} = (R_x, R_y, R_z)$ is the position of the basis centre. The angular momentum of this GTO is defined as the sum, $l = p+q+r$, where p,q and r are integer values in the range $[0, l]$.

In the molecular radicals, the spin wavefunction at a nucleus is described by the s-symmetry basis functions of that atom (basis functions of symmetry $l > 0$ do not contribute) and valence and/or diffuse basis functions of any symmetry from atoms in the vicinity. The contribution from the latter is relatively small compared to that from the former, therefore the accuracy of the results largely depends on the quality of core s-functions. This is particularly important when we use the standard form of $A_{\rm iso}$ employing the delta-function operator shown in equation (16). The GTO, unlike the STOs, do not fulfil the Kato cusp condition[158)] at the nucleus, thereby leading to errors in the spin-density at the nuclei. However the nuclear cusp condition can be approximated using contractions of s-symmetry GTOs with primitive GTOs containing large exponents, that is, with strongly peaked Gaussian orbitals. This can be achieved either using sufficiently extensive Gaussian basis-sets (with more exponents to describe the atomic orbitals of all symmetries), or by augmenting standard basis sets with additional tightly peaked s-symmetry GTOs.[159)] The latter may be preferred on computational grounds as the former approach can lead to unnecessarily large basis sets with extensive high-symmetry functions that are usually not needed in DFT calculations.

For the calculations on system like $H\cdot$,$H_2^+\cdot$ etc., the extremely contracted basis-set significantly increases the accuracy,[124)] and also the larger the valence basis-sets the more accurate the isotropic HFCC will be produced.[124,160)] However the calculations on intermediate or large systems must usually employ small or medium sized basis-sets for reasons of computational cost. For example, the Dunning basis-sets including cc-pVDZ, cc-pVTZ, cc-pVQZ (double, triple, quadruple-zeta, respectively) have a rigorously systematic expansion in terms of the number of exponents for one atomic orbital.[161,162)] They are optimised for the consistency to molecular correlation so therefore include polarisation functions, and can be augmented with diffusion functions (small ζ functions). We may expect a systematic improvement in the isotropic HFCCs as we use successively larger Dunning basis sets, but as these basis sets expand both the number of basis functions in a shell as well as the number of shells and the maximum symmetry of GTOs included, they expand in size quite dramatically and pose a prohibitive computational burden. On the other hand, basis sets like EPR-II and EPR-III are specifically optimised for the calculation of HFCCs by including s-orbitals with large exponents designed to better model the nuclear cusp.[123)] Likewise, the DGauss basis-sets, DGDZVP and DGDZVP2,[163)] are optimised for density functionals and also have very tightly peaked s-symmetry orbitals that can better describe the nuclear region. These basis sets are designed to better model the nuclear cusp without increasing the number of higher symmetry functions and are better suited for density functional calculations on large molecular systems.

5.2.3 Methods: density functionals

It is common that certain methods are selected simply due to their popularity. However, a better understanding of the level of theory that is being chosen can help interpret the underlying physics or chemistry. The basic principle of DFT is that the properties of the ground state of a many-particle system are uniquely determined by the electronic density (ρ), as shown by Hohenberg and Kohn,[164)] and this provides the ability to tackle the many-body problem of interacting electrons in a static external potential by reducing it to a tractable problem of non-interacting electrons with the same density distribution in an effective potential. Within this framework, the energy of the system is written as a unique functional of ρ, and in the KS framework,[165)] the energy is additionally expressed in terms of single-electron orbitals. While the major part of the functional are explicit in terms of the nuclei–electron and electron–electron Coulomb interactions, the remaining, unknown part, contains the approximation of the non-classical potential energy resulting from the exchange and correlation interactions, and also the difference between the kinetic energies of the KS system and the real interacting system. Therefore, a variety of levels of approximation may or may not handle different types of practical problems, mainly due to their different intrinsic flaws in the approximations.

The most basic class of approximations of xc functionals is the local density approximation (LDA), and the extension to spin-polarised systems termed the local spin-density approximation (LSDA). In the LSDA, the exchange-correlation energy functional is written as:[166)]

$$E_{xc}^{\rm LSDA}[\rho_\alpha, \rho_\beta] = \int \rho(\mathbf{r})\, \epsilon_{xc}(\rho_\alpha(\mathbf{r}), \rho_\beta(\mathbf{r}))\, {\rm d}^3\mathbf{r} \tag{20}$$

where $\rho = \rho_\alpha + \rho_\beta$ is the total electronic density and ρ_α and ρ_β are the spin up and down components. Here ϵ_{xc} denotes the one-particle exchange-correlation energy density for a uniform electron gas.[165,166)] The LDA/LSDA can be improved upon by including gradient corrections to yield the class of the approximations called the generalised gradient approximations (GGAs) which modify equation (20) by including a term that depends on $\nabla\rho_\alpha$ and $\nabla\rho_\beta$. There are many kinds of GGAs available, but the most common are BLYP,[167)] PW91[168)] and PBE.[169)] Of these, the former is an empirical functional, but in the PW91 and PBE functionals, all parameters are determined theoretically. It has been shown that the LSDA functional with gradient correction to the xc functional can help in the calculation of isotropic HFCCs of radicals.[120,121)]

Another class of functionals are the hybrid functionals which combine some fraction of Hartree–Fock (HF) exchange with local or semi-local exchange and correlation from GGAs. The Hartree–Fock non-local exchange energy is defined as

$$E_x^{\mathrm{HF}} = -\frac{1}{2}\sum_{i,j}\int \psi_i^*(\mathbf{r}_1)\psi_j^*(\mathbf{r}_1)\frac{1}{|\mathbf{r}_1-\mathbf{r}_2|}\psi_i^*(\mathbf{r}_2)\psi_j^*(\mathbf{r}_2)\,\mathrm{d}^3\mathbf{r}_1\,\mathrm{d}^3\mathbf{r}_2. \tag{21}$$

This term can be combined with the B88 exchange GGA,[167] the LYP correlation functional,[170] and the LDA with the VWN correlation functional[171] to yield one of the most commonly used functionals in quantum chemistry, the B3LYP hybrid functional:[172]

$$E_{xc}^{\mathrm{B3LYP}} = E_x^{\mathrm{LSDA}} + a_0(E_x^{\mathrm{HF}} - E_x^{\mathrm{LSDA}}) + a_x(E_x^{\mathrm{B88}} - E_x^{\mathrm{LSDA}}) + E_x{}^{\mathrm{LSDA}} + a_c(E_c^{\mathrm{LYP}} - E_c^{\mathrm{LSDA}}) \tag{22}$$

where the three parameters a_0, a_x and a_c are 0.20, 0.72 and 0.81 respectively. Another commonly used hybrid functional is PBE0[173] (also termed 'PBE1PBE') in which the PBE GGA is combined with HF exchange to yield:

$$E_{xc}^{\mathrm{PBE0}} = \frac{1}{4}E_x^{\mathrm{HF}} + \frac{3}{4}E_x^{\mathrm{PBE}} + E_c^{\mathrm{PBE}}. \tag{23}$$

Like PBE, PBE0 has been derived on theoretical grounds only and does not contain any parameters fitted to experimental data.

The density functionals discussed so far are either local, in the sense that the exchange-correlation energy density depends on the density at a point (LDA & LSDA), or semi-local if they include an additional dependence on the gradient at the point (GGAs). The hybrid functional additionally includes a partial non-locality through the HF exchange functional. However none of these functionals account for non-local correlation effects, and may only partially account for non-local exchange effects. Both shortcomings may be fixed by splitting the electron–electron interaction operator into a short-range (sr) part, which will be described using local or semi-local density functionals, and a long-range (lr) part, which will be described using Hartree–Fock or a higher level of theory.[174] This range separation is usually achieved using the error-function as follows:

$$\frac{1}{r_{12}} = \frac{1-\mathrm{erf}(\omega r_{12})}{r_{12}} + \frac{\mathrm{erf}(\omega r_{12})}{r_{12}}, \tag{24}$$

where the two terms account for the short and long range interactions, and ω is the parameter that controls the range separation. The use of error-function is due to the technical reason that the integrals with Gaussian basis functions can be solved analytically.[174] This leads to a class of long-range corrected (LC) hybrid xc functionals that are defined as

$$E_{xc}^{\text{LC-DFT}} = E_x^{\text{sr-DFT}}(\omega) + E_x^{\text{lr-HF}}(\omega) + E_c^{\mathrm{DFT}}. \tag{25}$$

Unlike a global hybrid functional (such as PBE0), where the exchange-correlation potential decays asymptotically as $-a/r$, where a is the fraction of HF exchange, the range-separated hybrid follows the exact $-1/r$ decay. The long-range correction in combination with the PBE exchange functional, denoted LC-ωPBE, is remarkably accurate for a broad range of molecular properties,[175] taking the form

$$E_{xc}^{\text{LC-wPBE}} = E_x^{\text{sr-PBE}}(\omega) + E_x^{\text{lr-HF}}(\omega) + E_c^{\mathrm{PBE}}. \tag{26}$$

Another commonly used range-separated functional that does not fit into the above paradigm is the CAM-B3LYP functional which employs two extra parameters, α and β, to define the exchange contributions of HF and DFT individually over the whole range. The 'CAM' stands for Coulomb-attenuating method. As a result of optimization of the two parameters, CAM-B3LYP comprises of 0.19 HF and 0.81 DFT exchange interaction at short-range, 0.65 HF and 0.35 DFT at long-range, and the correlation functional employed in B3LYP. This hybrid function containing long-range (LC) properties works well when dealing with the polarisability of long chains, excitation and charge transfer that B3LYP often failed to handle.[176] Some other LC hybrid density functionals include empirical atom-atom dispersion corrections and have been proven to be significantly superior for non-bonded interactions, such as wB97XD.[177]

For accurate isotropic HFCC calculations on organic systems we need a method that accurately describes both the spin-density from the SOMO and the spin polarization in the DOMOs. From the discussion above, we might expect that as we progress from the LDA, through the GGAs and hybrid and the LC functionals, we should expect a progressively higher accuracy in the calculations of A_{iso}. However this is not the case. As we have mentioned above, there are two contributions to the spin-density at the nuclei of open-shell species: the dominant contribution from the SOMO and another from the spin-polarization of the electrons in the DOMOs. In standard GGAs, the contribution from the SOMO is overestimated, but the inadequate local exchange leads to an underestimation of the contribution from the DOMOs. These effects partially cancel out, leading to relatively accurate values for the isotropic HFCCs.[122] However, as we shall demonstrate below, when we use hybrid or LC functionals, we fix the problem with the exchange, but this leads to larger errors in the isotropic HFCCs. This may suggest that part of the reason for good performance of the GGAs may be because of an error cancellation in the contributions from the SOMO and DOMOs. Improving the exchange functional only results in a breakdown of this error cancellation, and a poorer agreement with experiment.

5.2.4 Fermi contact operator

Compared with calculations of the isotropic HFCC (Fermi-contact term), DFT calculations of the anisotropic HFCC are comparatively easy due to the global nature of the operator (see equation (18)). The local nature of the isotropic HFCC gives rise to a high sensitivity to the accuracy of wave function at the sampling points, i.e. at the nuclear coordinates. Because the wavefunction is optimized to yield the best (ground state) energy — an integrated quantity — it does not follow that the wavefunction will be necessarily accurate at a particular point, unless that point contributes substantially to the energy. The electron–nuclear interaction is an important component to the total energy, but as long as the wavefunction around the nucleus is modelled accurately enough, this energy is not sensitive to the value of the wavefunction at the nucleus. This makes an accurate evaluation of A_{iso} difficult. In order to get rid of the error arising from the local sampling of the cuspless

wavefunction, we need to use an alternative form for $A_{\rm iso}$ that samples the wavefunction so as to average over errors in a vicinity around the nuclei. This is possible using the global operator forms of the Fermi-contact operator.[125–130)]

The derivation of the alternative operator is achieved using the hyper-virial theorem which states that for an arbitrary operator $\hat{W}$, if ψ_0 is eigenfunction of the Hamiltonian $\hat{H}$, then an alternative form for the delta function operator can be obtained:[125)]

$$\langle\psi_0|\delta(\mathbf{r})|\psi_0\rangle = \langle\psi_0|\hat{D}|\psi_0\rangle, \tag{27}$$

where the operator D is defined as

$$D = -\frac{1}{2\pi}r^{-3}\hat{L}^2 + \frac{m}{2\pi}\frac{\partial V}{\partial r}. \tag{28}$$

This equation can be further generalised to the N-electron case to yield the well-known HSF operator.[125,126)]

However, some investigations have shown that if the basis-sets are not sufficient, the HSF tend to generate incorrect spin or charge density at the sites of light nuclei that are in the vicinity of heavy atoms.[127,128)] Hence the requirement about size of basis-sets also causes the increase in the computational load.

In order to overcome the drawbacks of both delta and HSF operators, there are some new alternative operators using a Gaussian weighting function $F^G(r, r_0) = e^{-r^2/r_0^2}$ with a parameter r_0 to control the short and long range behaviour. It will be exactly the delta operator if $r_0 = 0$, and the HSF operator if $r_0 = \infty$, and the value in-between zero and infinity indicates the combination of both operators.[128,129)] A conclusive investigation with the Gaussian-weighted operator on aromatic radicals such as benzyl, 1-pyrolyl shows that the extension of basis-sets significantly improves the theoretical values of isotropic HFCC of heavy nucleus, while it has little effect on protons. For the calculation of large organic radicals, an optimum choice of the range parameter can help to recover the error of inadequate basis-sets.[130)] Despite the additional computational effort, the alternative Fermi-contact operators can be very useful to accurately determine isotropic HFCCs.

5.2.5 Vibrational contributions: harmonic

Vibrations of the molecules would cause a deviation to the isotropic HFCCs with respect to that of the static gas-phase molecules. The effects on the isotropic HFCC from the vibrations can be extremely large with motion of large amplitude.[178)] Though the vibrational corrections are computationally expensive and the lack of experimental quantification using gas-phase spectroscopy also makes it hard to benchmark the quality of the vibrational correction, it is still of considerable importance to take into account the molecular dynamics for its effect on the isotropic HFCC.

So far all the standard calculations on HFCCs are based on one optimised geometry. But in principle, even at 0 K, the 0^{th} order of harmonic vibrations in all normal modes are present, which give rise to a considerable amount of variation of $A_{\rm iso}$, due to the large sensitivity of the spin densities at the nuclear sites to the molecular geometry. In practice, it is the bond length between atom C and Mu that has the significant impact on the $A_{\rm iso}$.

The vibrational Hamiltonian can be written in terms of the normal coordinates Q_k, and the complete vibrational wave equation will have the form:[179)]

$$\frac{-h^2}{8\pi^2}\sum_{k=1}^{3N-6}\frac{\partial^2\psi_V}{\partial Q_k^2} + \frac{1}{2}\sum_{k=1}^{3N-6}\lambda_k Q_k^2\psi_V = E_v\psi_V \tag{29}$$

.

The normal coordinate of k^{th} vibrational mode, Q_k, is defined as $Q_k = \sum_i l_{ik}q_i$, where q_i is the mass weighted coordinate of atom i, and l_{ik} is the relative displacement in the mass-weighted coordinates and normalised to be 1.[179)] Then the wave equation (29) can be separated into $3N-6$ (the number of vibrational modes in a non-linear molecule of N atoms) equations in terms of one corresponding normal coordinate, so that the vibrational wave function can be written as

$$\psi_V = \psi(Q_1)\psi(Q_2)\psi(Q_3)\cdots\psi(Q_{3N-6}) \tag{30}$$

The solutions of the harmonic oscillator equation are the Hermite l functions and are in the form:

$$\psi_{\upsilon_k}(Q_k) = N_{\upsilon_k}e^{-\frac{1}{2}\gamma_k Q_k^2}H_{\upsilon_k}(\gamma_k^{\frac{1}{2}}Q_k) \tag{31}$$

where υ is the quantum number indicating the level of vibration and can be equal to any positive integer including 0, and the normalization factor N_{υ_k} takes the form,

$$N_{\upsilon_k} = [(\frac{\gamma}{\pi})^{\frac{1}{2}}\frac{1}{2^{\upsilon_k}(\upsilon_k)!}] \tag{32}$$

and γ_k takes the quantity $4\pi^2\upsilon_k/h$, and $H_{\upsilon k}(\gamma_k^{\frac{1}{2}}Q_k)$ is a polynomial of degree υ_k in Q_k.[179)]

For the full correction of the vibrationally averaged isotropic HFCC, the expectation value $\langle A_{\rm iso}\rangle_V$ is taken by,

$$\langle A_{\rm iso}\rangle_V = \frac{\langle\psi_V|A(Q_1, Q_2, ..., Q_{3N-6})|\psi_V\rangle}{\langle\psi_V|\psi_V\rangle}, \tag{33}$$

and for one specific mode it reduces to

$$\langle A_{\rm iso}\rangle_{\upsilon_k} = \frac{\langle\psi_{\upsilon_k}|A(Q_k)|\psi_{\upsilon_k}\rangle}{\langle\psi_{\upsilon_k}|\psi_{\upsilon_k}\rangle} \tag{34}$$

where $A(Q_k)$ is the $A_{\rm iso}$ as a function of the normal coordinate Q_k, which can be numerically calculated.

Since the population of any vibrational state ψ_{υ_k} is directly temperature-dependent in the system where the Boltzmann distribution is applied,[180)] the vibrationally averaged $A_{\rm iso}$ at temperature T is given by

$$\langle A_{\rm iso}\rangle_T = \sum_{k=1}^{3N-6}\sum_{\upsilon_k=0}^{\infty} f_{\upsilon_k}g_{\upsilon_k}\langle A_{\rm iso}\rangle_{\upsilon_k} \tag{35}$$

where g_{υ_k} is the degree of degeneracy of the vibrational level ψ_{υ_k}, and the corresponding Boltzmann factor f_{υ_k} is defined as[179)]

$$f_{\upsilon_k} = \frac{\exp(-E_{\upsilon_k}/k_{\rm B}T)}{\sum_{k=1}^{3N-6}\sum_{\upsilon_k} g_{\upsilon_k}\exp(-E_{\upsilon_k}/k_{\rm B}T)} \tag{36}$$

where $k_{\rm B}$ is the Boltzmann constant.

5.2.6 Vibrational effects: anharmonic

Muonium can be considered to be the light isotope of hydrogen,[181,182)] so that it is common that the muoniated organic radicals are studied as the perfect analogues of their H-substituted isotopomers. However the spin density of the electron at the muon site of muoniated radical is not the same

as that at the same proton site of the H-substituted analogue due to the isotope effect. This results in, according to the equation 15, the fact that the reduced muon HFCC in the muoniated radical, A'_μ ($A'_\mu = A_\mu\gamma_p/\gamma_\mu$, where A_μ here is the $A_{\rm iso}$ of the muon) is different from the $A_{\rm iso}$ of the proton of the H-substituted analogue. The difference mainly lies in the anharmonicity of the potential energy curve representing the vibrationally averaged structural parameters, among which the bond length is proven to be the most determinant one.[143,146] To take into account this isotope effect, one can calculate the vibrationally averaged geometry or even directly the averaged isotropic HFCC by employing the vibrational second order perturbation theory (V2PT). In practice, those calculations cost a large amount of time (the computational expense and the according results of muoniated benzene by V2PT will be tabulated in the Section 5.3), so that, for simplicity, the common way of achieving the anharmonic correction on isotropic HFCC is simply to calculate the bond stretch mode between the Mu and the carbon it attaches to. The basic idea is that the Mu is (much) lighter than the other atoms, one can assume that solely Mu is moving relatively to the other atoms. Moreover, as usually the most effective vibrational mode that influence the isotropic HFCC is C-Mu bond stretch, the system can be simply regarded as a diatomic system with a stretching along the C-Mu bond.

The potential energy surface (PES) as function of C-Mu bond length normally shows an asymmetry with a morse-potential feature. The straightforward method is to fit the PES to a morse potential $V(x)$:

$$V(x) = D_e(1 - e^{-a(x-x_e)})^2 \tag{37}$$

where x is the distance between the two atoms, x_e is the equilibrium bond distance, D_e and a defines the depth and 'width' of the potential well, respectively.

The analytic nth-order wave function accordingly given by

$$\Psi_n(z) = N_n z^{\lambda-n-\frac{1}{2}} e^{-\frac{1}{2}z} L_n^{2\lambda-2n-1}(z) \tag{38}$$

where the $z = 2\lambda e^{-(x-x_e)}$, $N_n = n![\frac{2\lambda-2n-1}{\Gamma(n+1)\Gamma(2\lambda-n)}]^{\frac{1}{2}}$; $L_n^\alpha(z)$ is a laguerre polynomial function of z, and is equal to 1 if n=0.

The matrix elements of the vibrationally averaged bond length $\langle x\rangle_m$ in state m is given by

$$\langle x\rangle_m = \langle\Psi_m(x)|x|\Psi_m(x)\rangle, \tag{39}$$

and the vibrationally averaged isotropic HFCC $\langle A_{\rm iso}\rangle_m$ is given by:

$$\langle A_{\rm iso}\rangle_m = \langle\Psi_m(x)|A(x)|\Psi_m(x)\rangle, \tag{40}$$

where the $A_{\rm iso}(x)$ is the isotropic HFCC as a function of bond length x.

For a system in its ground vibrational state, $m = 0$, we define the averaged bond length, $\langle x\rangle_0$, the averaged isotropic HFCC $\langle A_{\rm iso}\rangle_0$, and we may also define the isotropic HFCC evaluated at the vibrationally averaged bond length, $A_{\rm iso}(\langle x\rangle_0)$. Since the isotropic HFCC is generally quite sensitive to the basis set used, and the optimised and the vibrationally averaged geometry is generally less sensitive to the quality of basis set, we may employ a small basis set to average the geometry to obtain $\langle x\rangle_0$, and subsequently evaluate $A_{\rm iso}(\langle x\rangle_0)$ using a larger basis set. We will explore this possibility in the following sections.

Vibrational 2nd-order perturbation theory (V2PT)[183] is an alternative and commonly used method to calculate the anharmonicity and have an overall approximation for all the atoms in the system. The anharmonicity is included as a perturbation of the harmonic oscillator,

$$\hat{H}_{V2PT} = \hat{H}_{HO} + \hat{H}_{Anharm} \tag{41}$$

where the harmonic oscillator $\hat{H}_{HO}$ is the zeroth order Hamiltonian and the $\hat{H}_{Anharm}$ include the cubic and quartic force constants which are the direct derivative by numerical differentiation of any analytical Hessian:

$$\hat{H}_{Anharm} = \sum_{ijk} f_{ijk}q_iq_jq_k + \sum_{lmno} f_{lmno}q_lq_mq_nq_o. \tag{42}$$

The method can normally produce reasonably accurate results, although it is only applicable when the harmonic term dominates. Despite its high expense in the numerical Hessian calculation, it provides satisfying low order PES approximations.

5.3 Numerical examples of the methodology

We now present some examples of the methodological issues associated with the isotropic HFCC calculations described above. All the calculations presented here have been carried out using the Gaussian09 package,[184] which is the most commonly used code applied to μSR. We proceed by performing the different levels of DFT calculations and vibrational corrections for some typical muoniated radicals and their protonated species with the parental molecules. These examples are presented in Figure 18 and include benzene(C_6H_6), naphthalene($C_{10}H_8$), pyrene($C_{16}H_{10}$) and TIPS-pentacene($C_{16}H_{10}Si_2$, also known as 6,13-Bis(triisopropylsilylethynyl)pentacene).

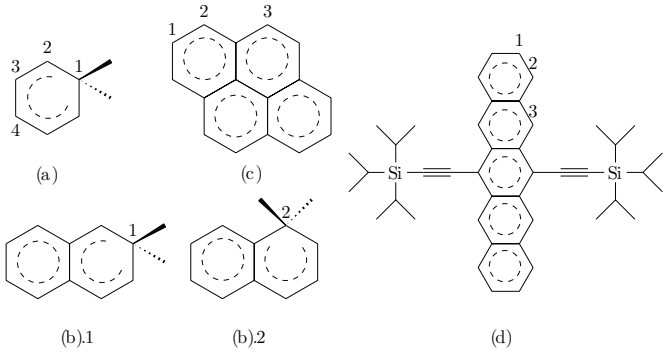

Fig. 18. (a) Muonium-substituted cyclohexadienyl, C_6H_6Mu, and the assignment of the carbons where four non-equivalent hydrogens are bonded; (b) Naphthalene ($C_{10}H_8$) and the assignment of two sites where the Mu/H can be added, and the muoniated naphthalene radical is then 1-Mu-naphthyl and 2-Mu-naphthyl for site 1 and 2 addition, respectively; (c) Pyrene($C_{16}H_{10}$) and the assignment of three sites where the Mu/H can be added, and the corresponding muoniated pyrene radical is then 1-Mu-pyrenyl, 4-Mu-pyrenyl and 2-Mu-pyrenyl for site 1, 2 and 3 addition, respectively; (d) TIPS-pentacene($C_{16}H_{10}Si_2$) and the assignment of three sites where the Mu/H can be added. The corresponding muoniated TIPS-pentacene radical is then 6,13-bis(triisopropylsilylethynyl)-2-Mu-pentacenyl, 6,13-bis(triisopropylsilylethynyl)-1-Mu-pentacenyl and 6,13-bis(triisopropylsilylethynyl)-5-Mu-pentacenyl for site 1, 2 and 3 addition, respectively. (There are two more addition sites on the triple bond, which are not going to be discussed in this article, hence not labeled in the figure.)

5.3.1 *Variations with basis set*

Cyclohexadienyl (C_6H_7) provides an ideal testing ground for the basis-set sensitivity of the isotropic HFCC as for this system, the isotropic HFCC is relatively insensitive to the density functional used (see results presented in Section 5.3.2), thus we are able to decouple these two effects. An important consideration for any electronic structure calculation is the computational resource needed. In Table I we present the real computational time (CPU time) needed for the geometry optimization and single-point energy calculations on this system as a function of basis set. In all calculations the B3LYP functional has been used. The calculation of isotropic HFCC for the protons in C_6H_7 with the two hydrogen atoms attached to the same carbon are equivalent vibrationally. Here there seems to be little effect from anharmonicity, and the results may be compared directly to the experimental data of C_6H_7 from EPR measurements.

From Table I we see that, for the sequence of Dunning basis sets, there is a consistent increase in the isotropic HFCC, $A_{\rm iso}$, as the basis size increases. This has been observed in other studies on small radicals[124, 160] and is consistent with the discussion in Section 5.2.2 on the sensitivity of the isotropic HFCC to the nuclear cusp: as we move up the Dunning basis series, the nuclear cusp is better described, and the spin-density at the nucleus seems to converge relatively smoothly. We also see that the results of both $A_{\rm iso}$ and the C–H bond length from the DGauss and EPR-III basis-sets are comparable to those from the (aug)-cc-pVQZ basis-sets. This seems to be the case as these basis sets have comparable s-symmetry contractions. This is an encouraging result as the DGauss basis sets are considerably smaller that both the EPR-III and Dunning quadruple-ζ basis sets.

It is noticeable that except for the double-ζ basis sets, the theoretical results for the isotropic HFCC all exceed the experiment value. This may be due to many factors, among which, however, the most dominant may be the intrinsic overestimation of the SOMO wave-function at the nuclear positions.[122] It is also worth noting that the difference of the bond-length optimised by the cc-pVDZ and aug-cc-pVDZ basis sets from that by the cc-pVQZ basis. The isotropic HFCC is very sensitive to the lengths of C–Mu and C–H bonds, so we cannot recommend that the Dunning double-ζ basis sets be used for geometry optimisation. However, both of the DGauss basis sets, though smaller in size, seem to yield better geometries. We will look deeper into this matter in Sections 5.3.3.2 and 5.3.3.3 where we will discuss the effects of anharmonic vibrations.

Basis-set	CPU time		$A_{\rm iso}(R_e)$	R(C – H)
	opt	sp	MHz	Å
DGDZVP	1 min	15 s	147.05	1.1045
DGDZVP2	1.2min	15 s	145.69	1.1044
cc-pVDZ	1.5 min	15 s	127.80	1.1122
aug-cc-pVDZ	9 min	1 min	128.36	1.1093
cc-pVTZ	21 min	3 min	140.95	1.1036
EPR-III	38 min	5 min	148.56	1.1034
aug-cc-pVTZ	3 h	15 min	138.76	1.1035
cc-pVQZ	5.7 h	20 min	142.57	1.1023
aug-cc-pVQZ	45 h	2 h	142.95	1.1029
C_6H_7 Exp.[185]			134.63	—

Table I. Summary of the computational (CPU) time per core on the Mid-Plus Aprocrita system with Intel Xeon E5645 (Westmere) cores. Theoretical isotropic HFCCs are calculated at the equilibrium bond lengths, $A_{\rm iso}(R_e)$, and bond-length, R(C – H), of carbon and the out-of-plane hydrogen in C_6H_7 (cyclohexadienyl), at the geometries optimised by using the B3LYP density functional with a range of basis-sets. The CPU times for the geometry optimisation (denoted as 'opt') and single-point energy calculation (denoted as 'sp') are listed for each basis-set. The CPU times are roughly proportional to the cube of the basis size.

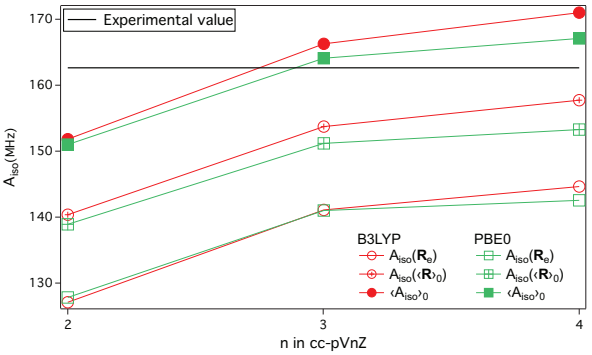

Fig. 19. (Color online) The isotropic HFCC for the muon in C_6H_6Mu (Mu-substituted cyclohexadienyl) evaluated at the equilibrium geometry, $A_{\rm iso}(R_e)$, at the vibrationally averaged C–Mu bond length, $A_{\rm iso}(\langle R\rangle_0)$, and vibrationally averaged in the ground vibrational state, $\langle A_{\rm iso}\rangle_0$. Vibrational averaging was done with a Morse potential as described in the text, with equation 39 and 40. The Dunning basis sets used are indicated as cc-pVnZ, where $n = 2, 3$ and 4 indicate the cc-pVDZ, cc-pVTZ and cc-pVQZ basis sets respectively.

H site	Functional	$A_{\rm iso}(R_e)$	$A_{\rm iso}^{\rm Expt}$
1	B3LYP	142.57	134.61±0.06
	CAM-B3LYP	138.52	
2	B3LYP	−29.56	25.22±0.06
	CAM-B3LYP	−27.64	
3	B3LYP	11.99	7.54±0.06
	CAM-B3LYP	11.75	
4	B3LYP	−39.32	36.83±0.06
	CAM-B3LYP	−37.18	

Table II. Comparison of theoretical isotropic HFCCs of the protons evaluated at the equilibrium geometry, i.e. $A_{\rm iso}(R_e)$, at the theory level of B3LYP and CAM-B3LYP with the same basis-set cc-pVQZ. $A_{\rm iso}(R_e)$ and $A_{\rm iso}^{\rm Expt}$ denote the theoretical and experimental[185] isotropic HFCCs of the protons on different sites in the cyclohexadienyl, C_6H_7 (the assignment of sites are shown in Figure 18 (a)). The isotropic HFCCs are reported in MHz.

5.3.2 *Variations with density functional*

The B3LYP and PBE0 are probably the most popular and versatile hybrid functionals currently in use. From Figure 19 we see that these functionals produce very similar isotropic HFCCs for the muoniated benzene radical system. In Tables II and III we present data for the muoniated benzene, naphthalene, and pyrene radicals. These calculations have been performed with both the B3LYP functional as well as the range-separated CAM-B3LYP functional, but, for these systems, there seems to be little or no effect of the range-separation on the isotropic HFCCs.

TIPS-pentacene is a large, heavily delocalised molecule for which we may expect the effect of range-separation to be quite large. Indeed this is the case, and as we see from the data pre-

$C_{10}H_8Mu$	Functional	$A_{iso}(R_e)$	A_{iso}^{Expt}
Site 1	B3LYP	100.38	112.07±0.01
	CAM-B3LYP	100.04	
Site 2	B3LYP	121.04	137.13±0.01
	CAM-B3LYP	120.41	

$C_{16}H_{10}Mu$	Functional	$A_{iso}(R_e)$	A_{iso}^{Expt}
Site 1	B3LYP	72.80	82.63±0.01
	CAM-B3LYP	78.37	
Site 2	B3LYP	97.30	109.01±0.01
	CAM-B3LYP	97.07	
Site 3	B3LYP	149.11	166.82±0.01
	CAM-B3LYP	148.02	

Table III. Comparison of theoretical values of the reduced isotropic HFCCs of muons evaluated at the equilibrium geometry, i.e. $A_{iso}(R_e)$, at the theory level of B3LYP and CAM-B3LYP with the same basis-set cc-pVTZ. The A_{iso}^{Expt} is the experimental value of the reduced isotropic HFCC of muon in the muoniated naphthalene($C_{10}H_8Mu$) and muoniated pyrene($C_{16}H_{10}Mu$) for different Mu adduct sites. The assignment of sites are shown in Figure 18 (b) and (c).[186,187] The isotropic HFCCs are reported in MHz.

Basis set	Functional		
	B3LYP	CAM-B3LYP	wB97XD
$A_{iso}(R_e)[Mu^+]$ (MHz)			
cc-pVDZ	76.81	99.37	87.78
DGDZVP	87.93	113.96	104.26
DGDZVP2	89.96	115.65	103.20
Exp*[188]		80.5±0.1	
$A_{iso}(R_e)[\alpha - H^+]$ (MHz)			
cc-pVDZ	24.84	32.10	29.85
DGDZVP	28.37	36.45	32.76
DGDZVP2	28.68	36.78	34.16
Exp*[189]		19.3±0.1	

Table IV. Comparison of theoretical isotropic HFCCs, $A_{iso}(R_e)$, of the muon and the α-proton in the muoniated TIPS-pentacene with site-3 (6,13-bis(triisopropylsilylethynyl)-5-Mu-pentacenyl, also see assignment in Fig. 18 (d)), calculated using B3LYP, CAM-B3LYP and wB97XD, with the basis sets cc-pVDZ, DGDZVP and DGDZVP2. The experimental values for the muoniated TIPS-pentacene with the same addition site are taken experimentally from Reference.[188,189]

sented in Table IV where we have additionally included data from the range-separated wB97XD[177] functional. Here we see that both range-separated functionals result in isotropic HFCCs that differ quite substantially from those from the hybrid B3LYP functional. This difference may be attributed to the substantial increase in the non-local Hartree–Fock exchange included in CAM-B3LYP and wB97XD. However this inclusion seems to cause these more advanced functionals to deviate even more from the experimental data. This is a manifestation of the fortuitous error cancellation seen in standard density functionals which is discussed at the end of Section 5.2.3. When we improve the exchange functional to correct the spin polarization in the system, the overestimation of the SOMO contribution causes a corresponding overestimation of A_{iso}. This may suggest that we should not use range-separated functionals to calculate the HFCCs, but this is unsatisfactory as there are clear theoretical reasons to use range-separation to improve the treatment of electron exchange in delocalised systems. Clearly more work needs to be done to provide an adequate solution to this problem.

5.3.3 Vibrational corrections

So far we have evaluated the isotropic HFCC using equilibrium molecular geometries. That is, we have evaluated $A_{iso}(R_e)$. As we have discussed in Sections 5.2.5, and 5.2.6, due to the light mass of the muon, vibrational quantum effects are expected to be large and must therefore be included. Here we will calculate these effects using the approximations discussed above to evaluate the isotropic HFCC at the vibrationally averaged structure, $A_{iso}(\langle R\rangle_0)$, as well as the fully vibrationally averaged isotropic HFCC, $\langle A_{iso}\rangle_0$.

5.3.3.1 Harmonic vibrational corrections Vibrational averaging with the nuclear wavefunction in the harmonic approximation does not alter the average molecular geometry, i.e., $R_e = \langle R\rangle_{0,Harm}$, but, due to the asymmetry of A_{iso} about the equilibrium geometry as shown in Figure 20, $\langle A_{iso}\rangle_{0,Harm} \neq A_{iso}(R_e)$. The vibrational modes corresponding to the C–Mu stretch normally arise at fairly high frequencies due to the small muon mass. The effects of some of these modes on A_{iso} for the C_6H_6Mu molecule are shown in Table V. It can be seen that, within the harmonic approximation, although we do see an increase in A_{iso}, particularly for the muon, the increase is not sufficient, and does not bring the vibrationally averaged isotropic HFCC in agreement with experiment. The highest frequencies ($k = 32$ and 33), have the largest effect on the muon isotropic HFCC, but the effect is still relatively small. For the temperature dependent averaging of the isotropic HFCC, the higher vibrational levels at those modes will be merely populated at room temperature. While on the other hand, though the higher vibrational levels of the lower frequency mode could be considerably populated, the variation of HFCC is small. It has to be also noted here that, for molecular systems with more atoms, the frequencies of the vibrational modes with the lowest zero-point energies tend to be lower. Therefore for those vibrational modes, more energy levels can be excited with temperature and then contribute to the averaging for the isotropic HFCCs. The more vibrational modes that are taken into account, the more accurate the harmonic correction can be. However, some modes tend to increase the HFCC while the others tend to decrease them, which may result in a cancellation from all the contributions, or lead to a very small variation in the HFCCs. Hence we conclude that though including nuclear vibrational effects through the harmonic approximation may seem like a reasonable and computationally cheap way of including vibrational contributions to A_{iso}, in practice this approach results in a very small effect and is probably not worth performing.

5.3.3.2 Anharmonic vibrational corrections: the Morse potential As discussed in Section 5.2.6, the simplest way of including the effects of anharmonic nuclear vibrations on A_{iso} is to model the C–Mu stretch using a one dimensional Morse potential.[146] In this approach we may leave the other atoms fixed at their equilibrium positions, and change only the position of the Mu atom. This is probably valid because of the light mass of the muon.[146] Since the wavefunctions of the Morse oscillator can be obtained analytically, the vibrationally averaged isotropic HFCC, $\langle A_{iso}\rangle_{0,Morse}$, can be evaluated easily by sampling the Morse wavefunction and A_{iso} on a one-dimensional grid of points. In Table VI we report

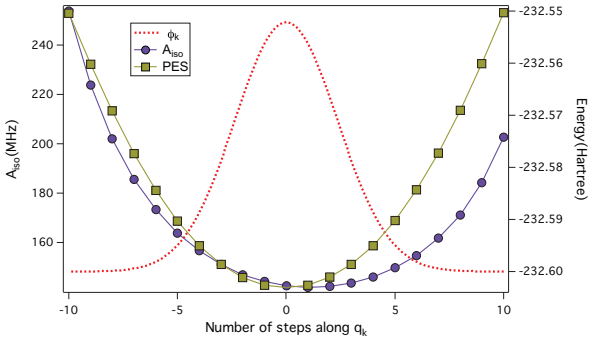

Fig. 20. (Color online) The HFCC of Mu, $A_{\rm iso}$, and potential energy V as a function of the steps along the $k = 32$ normal coordinate of C_6H_6Mu. The corresponding harmonic potential wave function $\phi_{k=32}$ is also indicated by the red dash curve. The calculation is down at the theory level of PBE0/cc-pVQZ.

Normal coordinate (k)	Frequency cm^{-1}	$\langle A_{\rm iso}\rangle_k$ MHz Mu^+	α–H^+
1	183.9	142.39	142.59
2	386.2	142.59	142.79
3	546.8	140.42	141.68
31	3359.3	144.82	143.33
32	3422.0	145.34	142.90
33	8513.3	145.58	142.48
$A_{\rm iso}(R_e)$	—	142.57	142.76
Exp.[132]	—	161.2±0.01	127.11±0.04

Table V. The harmonic ZPE average of isotropic HFCC $A_{\rm iso}$ along of Mu^+ and α-H^+ along the k-th normal coordinate of the C_6H_6Mu molecule. The non-averaged isotropic HFCCs, $A_{\rm iso}(R_e)$ and the experimental results are also shown. All the calculations done at the theory level of PBE0/cc-pVQZ.

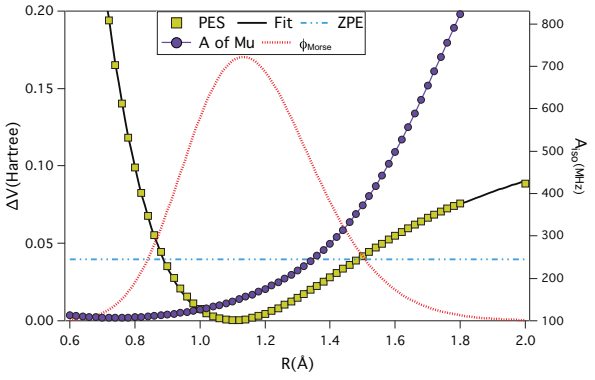

Fig. 21. (Color online) The muon isotropic HFCC, $A_{\rm iso}$ of the C_6H_6Mu molecule, as a function of the C–Mu stretch coordinate R together with the computed potential energy surface (PES), and the Morse potential fit. Also indicated is the zero point energy (ZPE) and the wavefunction of the lowest vibrational state in the Morse potential.

the muon isotropic HFCC for C_6H_6Mu calculated with this approach using a variety of basis sets. Firstly we see that both $\langle A_{\rm iso}\rangle_{0,\rm Morse}$ and $A_{\rm iso}(\langle R\rangle_{0,\rm Morse})$ yield substantially larger isotropic HFCCs compared with both $A_{\rm iso}(R_e)$ and the harmonically averaged isotropic HFCC, $\langle A_{\rm iso}\rangle_{0,\rm Harm}$. Secondly, we see that $\langle A_{\rm iso}\rangle_{0,\rm Morse} > A_{\rm iso}(\langle R\rangle_{0,\rm Morse})$. This should be expected from the behaviour of $A_{\rm iso}$ as a function of R(C–Mu)

Basis set	$A_{\rm iso}(R_e)$	$A_{\rm iso}(\langle R\rangle_{0,\rm Morse})$ MHz	$\langle A_{\rm iso}\rangle_{0,\rm Morse}$	$\langle R\rangle_{0,\rm Morse}$ Å
cc-pVDZ	127.80	140.12	145.28	1.164
aug-cc-pVDZ	128.35	139.85	144.55	1.161
cc-pVTZ	140.95	152.42	156.92	1.154
aug-cc-pVTZ	138.76	150.21	154.81	1.154
cc-pVQZ	142.57	154.59	159.55	1.153
aug-cc-pVQZ	142.95	153.59	167.29	1.153
DGDZVP	147.05	159.32	172.90	1.155
DGDZVP2	145.69	157.35	170.66	1.154
EPR-III	148.56	159.80	174.09	1.154
Exp.[132]		161.20±0.01		—

Table VI. A comparison of the theoretical isotropic HFCC of C_6H_6Mu computed with different basis sets with and without averaging using the Morse potential wavefunction. The vibrationally averaged C-Mu bond length $\langle R\rangle_{0,\rm Morse}$ with different basis sets is also tabulated. All the calculations are done by using the PBE0 hybrid functional.

shown in Fig. 21. Not surprisingly, the heavily contracted basis sets (DGDZVP, DGDZVP2 and EPR-III) tend to produce higher isotropic HFCCs than the Dunning basis sets. As before, the Dunning basis sets result in a systematically increasing isotropic HFCC, both $\langle A_{\rm iso}\rangle_{0,\rm Morse}$ and $A_{\rm iso}(\langle R\rangle_{0,\rm Morse})$, which appear to be converging at the quadruple-ζ basis set. This data is graphically displayed in Fig. 19 where we show calculations from both B3LYP and PBE0. The averaged C–Mu bond length of the muoniated benzene, $\langle R\rangle_{0,\rm Morse}$, is consistent with the value of 1.16 Å obtained from the undamped dynamical approach.[145] This could mean that the one-dimensional Morse approximation is adequate.

In Tables VII we present similar data for the muoniated naphthalene and pyrene radicals, but this time using only the cc-pVTZ and EPR-III basis sets. Broadly, the results for these systems are similar as those observed for muoniated benzene. The general conclusion that we can draw is that, for large enough basis sets, $A_{\rm iso}(R_e) < A_{\rm iso}(\langle R\rangle_{0,\rm Morse}) \lesssim A_{\rm iso}^{\rm Expt} < \langle A_{\rm iso}\rangle_{0,\rm Morse}$.

The vibrationally averaged C-Mu bond length $\langle R\rangle_{0,\rm Morse}$ shown in the Table VI is very consistent to the value, 1.16Å, obtained by the undamped dynamical approach of simulation the C-Mu bond-stretching vibrations by displacing the Mu from its equilibrium position in the C-Mu bond direction,[145] which probably means that the approximation of the bond-length by the Morse-potential fit is good enough.

However, given the fact that the TZ/QZ basis-set already produce exceeding isotropic HFCC according to the Table I, the only reason that the results from TZ/QZ basis-set by this approach happen to be around the literature value rather than exceeding it (shown in the Table VI), would be that this Morse-potential approximation actually fails to take account the slightly reduced C-H bond length.[144] So that the unpaired electron density may be more distributed at the α-proton at the geometry with only C–Mu bond-length increased, than that at the geometry with both C–Mu bond-length increased and corresponding C–H bond-length decreased, and in turn less distributed at the muon. Therefore, this approach can only partially correct the isotropic HFCC of muon, but not for the other nuclei. Nevertheless, it is producing rather good correction for muon isotropic HFCC.

Site	Basis set	$A_{\rm iso}^{\rm Expt}$	$A_{\rm iso}(R_{\rm e})$	$A_{\rm iso}(\langle R\rangle_{0,\rm Morse})$	$\langle A_{\rm iso}\rangle_{0,\rm Morse}$
			$C_{10}H_8Mu$		
1	cc-pVTZ	112.07	100.38	107.93	117.61
	EPR-III	±0.02	107.18	115.54	126.25
2	cc-pVTZ	137.13	121.04	130.03	142.21
	EPR-III	±0.06	129.79	139.83	153.28
			$C_{16}H_{10}Mu$		
1	cc-pVTZ	82.76	76.80	83.15	90.43
	EPR-III	±0.01	82.25	89.25	97.33
2	cc-pVTZ	109.04	97.30	101.11	105.20
	EPR-III	±0.01	104.45	108.70	113.28
3	cc-pVTZ	166.67	149.11	160.70	175.76
	EPR-III	±0.02	159.90	172.82	189.46

Table VII. The comparisons of theoretical isotropic HFCCs in muoniated naphthalene and pyrene ($C_{10}H_8Mu$ and $C_{16}H_{10}Mu$) with different basis-sets via Morse-potential fit corrections. The $A_{\rm iso}(R_{\rm e})$, $A_{\rm iso}(\langle R\rangle_{0,\rm Morse})$ and $\langle A_{\rm iso}\rangle_{0,\rm Morse}$ denote the muon isotropic HFCCs from the calculations by considering the Mu equivalent to H, by evaluation at the vibrationally averaged geometry/bond-length and by the directly averaging of isotropic HFCC, respectively. All the calculations are done by using the PBE0 hybrid functional. The $A_{\rm iso}^{\rm Expt}$ is the experimental value of the reduced isotropic HFCC of muon for different Mu adduct sites.[186,187] The assignment of Mu sites are shown in Figure 18 (b) and (c). The isotropic HFCCs are reported in MHz.

Basis-set	Mu^+	$\alpha-H^+$	$2-H^+$	$3-H^+$	$4-H^+$
			$A_{\rm iso}(\langle\{R_i\}\rangle_{0,\rm V2PT})$		
cc-pVDZ*	157.57	133.70	-26.06	9.54	-34.23
DGDZVP*	151.59	130.00	-26.07	9.56	-34.32
cc-pVTZ*	156.63	131.75	-25.67	9.29	-34.08
			$\langle A_{\rm iso}\rangle_{0,\rm V2PT}$		
cc-pVDZ	148.87	121.04	-26.51	10.42	-33.85
DGDZVP	169.85	139.40	-30.10	11.45	-39.08
cc-pVTZ	164.77	132.90	-26.17	10.43	-33.33
Exp.[132]	161.2	127.11	-24.14	8.47	-35.19
Err.	±0.01	±0.04	±0.04	±0.04	±0.04

Table VIII. The comparison of the theoretical isotropic HFCCs of muon and all different protons (see assignment of different protons are shown in Figure 18 (a)) in the muoniated benzene radical (C_6H_6Mu) with different basis-sets, via the V2PT ZPE corrections. All the calculations are done with the PBE0 functional. The isotropic HFCCs are reported in MHz.
*The basis-sets are only employed in averaging the strucuture, $\langle\{R_i\}\rangle_{V2PT}$, and all the final results of isotropic HFCC denoted as $A_{\rm iso}(\langle\{R_i\}\rangle_{0,\rm V2PT})$ is evaluated at the theory level of PBE0/cc-pVTZ.

Basis-set	$C_{10}H_8Mu$ Site 1	$C_{10}H_8Mu$ Site 2
	$A_{\rm iso}(\langle\{R_i\}\rangle_{0,\rm V2PT})$	
cc-pVDZ*	113.65	132.45
DGDZVP*	109.63	127.71
	$\langle A_{\rm iso}\rangle_{0,\rm V2PT}$	
cc-pVDZ	106.04	124.48
DGDZVP	121.23	142.84
cc-pVTZ	N.C.	N.C.
Exp.[186]	112.07±0.02	137.14 ± 0.06

Basis-set	$C_{16}H_{10}Mu$ Site 1	Site 2	Site 3
		$A_{\rm iso}(\langle\{R_i\}\rangle_{0,\rm V2PT})$	
cc-pVDZ*	84.40	109.31	166.02
		$\langle A_{\rm iso}\rangle_{0,\rm V2PT}$	
cc-pVDZ	79.02	100.01	156.31
cc-pVTZ	N.C.	N.C.	N.C.
Exp.[187]	82.76±0.01	109.04±0.01	166.67±0.01

Table IX. The comparison of the isotropic HFCCs for the muoniated naphthalene ($C_{10}H_8Mu$) and pyrene ($C_{16}H_{10}Mu$) radicals at different Mu-adduct sites (see assignment of sites in Fig. 18 (b) and (c)) by different V2PT correction schemes, and all the calculations are done with the PBE0 functional. The isotropic HFCCs are reported in MHz.
*The basis-sets are only employed in averaging the strucuture, $\langle\{R_i\}\rangle_{0,\rm V2PT}$, and all the final results of isotropic HFCC denoted as $A(\langle R\rangle_{V2PT})$ is evaluated at the theory level of PBE0/cc-pVTZ.

5.3.3.3 Anharmonic vibrational corrections: V2PT

The vibrational 2nd perturbation theory is very computationally expensive, though it can achieve accurate results. Other than the Morse potential fitting approach that only modifies the isotropic HFCC of Mu, it corrects the values for all the protons/muon in the system. A good result is obtained for muoniated benzene is obtained with the basis set cc-pVTZ, which is compared to the results with other basis sets in the Table VIII. It is a conclusive fact that the value of $A_{\rm iso}(\langle\{R_i\}\rangle_{0,\rm V2PT})$ is produced smaller than the $\langle A_{\rm iso}\rangle_{0,\rm V2PT}$ with the same basis-set (cc-pVTZ), similar to that the $A_{\rm iso}(\langle R\rangle_{0,\rm Morse})$ is always smaller than the $\langle A_{\rm iso}\rangle_{0,\rm Morse}$.

Due to the substantial expense in this numerical calculation, the smaller basis sets such as cc-pVDZ and DGDZVP can be employed to calculate the anharmonic vibrational averaging of the geometry, $\langle\{R_i\}\rangle_{0,\rm V2PT}$, under the assumption that the $\langle\{R_i\}\rangle_{0,\rm V2PT}$ is less sensitive to the basis sets. The isotropic HFCC can then be evaluated by the single point calculation with better basis set such as cc-pVTZ, that is, $A_{\rm iso}(\langle\{R_i\}\rangle_{0,\rm V2PT})$. Table VIII summarises the $A_{\rm iso}(\langle\{R_i\}\rangle_{0,\rm V2PT})$ and $\langle A_{\rm iso}\rangle_{0,\rm V2PT}$ for the muon and all the other protons. There is little difference in the $A_{\rm iso}(\langle\{R_i\}\rangle_{0,\rm V2PT})$ that are all calculated with the same cc-pVTZ but based on the averaged geometries, $\langle\{R_i\}\rangle_{0,\rm V2PT}$ with different basis sets (cc-pVDZ, DGDZVP and cc-pVTZ), which indicates the insensitivity of $\langle\{R_i\}\rangle_{0,\rm V2PT}$ to the basis sets.

For the larger systems such as muoniated naphthalene and pyrene radicals, the averaging of geometry via V2PT with cc-pVTZ will not converge. The good results of $A_{\rm iso}(\langle\{R_i\}\rangle_{0,\rm V2PT})$ in the Table IX shows that it is a feasible way to do the V2PT correction is to calculate the averaged geometry, $\langle\{R_i\}\rangle_{0,\rm V2PT}$ with smaller basis-sets, such as cc-pVDZ or DGDZVP, and then calculate the $A_{\rm iso}(\langle\{R_i\}\rangle_{0,\rm V2PT})$ with bigger basis-set such as cc-pVTZ.

The Table VIII and IX both show incredibly good results from $A_{\rm iso}(\langle\{R_i\}\rangle_{0,\rm V2PT})$ with cc-pVTZ no matter what basis sets are employed for the geometry averaging. However, the $\langle A_{\rm iso}\rangle_{0,\rm V2PT}$ solely by cc-pVDZ gives underestimated results due to the sensitivity of isotropic HFCC to the basis set size, while the DGDZVP tend to overestimate the results due to the artificially heavily contracted s orbital. Since the $\langle A_{\rm iso}\rangle_{0,\rm V2PT}$ can not be obtained with cc-pVTZ for systems like muoniated naphthalene and pyrene, it is advisable to calculate the $A_{\rm iso}(\langle\{R_i\}\rangle_{0,\rm V2PT})$ instead.

6. Conclusions

It seems very clear that muons have a significant role to play in understanding charge and spin dynamics in organic materials. However, it is likely that the use of charge carrier motion models to interpret the low-field relaxation rate data in these systems needs to be revisited. Independent of whether a neutral soliton or charged polaron are supported by the molecular structure, the magnetic field dependent relaxation rate data seems to show consistency with what would be expected from charge carrier motion. However, there is very clear evidence for ALC resonances in a number of materials, which points towards a localised state. Moreover, whilst it is a somewhat inaccurate method to estimate HFCCs, the depolarising asymmetry in almost all materials studied also follows a trend that points towards localised electronic states; we note this is also independent of whether a polaron or soliton is supported. We are therefore left hunting for an appropriate localised model that can explain the field dependence of the relaxation rate data present in the majority of organic materials.

As previously asked, could electron spin relaxation be the major part of the muon spin relaxation rate, which was previously attributed to charge carrier dynamics[73–84,97,99,100]? If so, the field dependence would come from the gradual decoupling of the various mechanisms that cause electron spin relaxation - for example, the hyperfine and spin orbit interactions. The decoupling fields and the temperature dependence of these two interactions could be different, and could therefore conspire together to mimic the field and temperature dependent relaxations expected from the charge carrier motion models. There may also be a non-exponential relaxation rate as a result of the superposition of signals from multiple sources, thus confusing the issue considerably.

Perhaps a solution to the problem interpreting low-field relaxation rates lies in a detailed and careful experimental investigation of the muonium states in a relatively simple organic semiconductor, such as the acenes. In particular, the role of hyperfine interaction on the muon's spin relaxation can be assessed by measuring deuterated and hydrogenated semiconductors. Applying a small magnetic field (less than 5 G) would decouple the direct muon-nucleon HFI, followed by a subsequent the electron-nucleon HFI decoupling at higher fields, and an eventual muon-electron HFI decoupling at higher fields still. Yet, spin orbit interaction would tend to increase as the magnetic field is increased. Studies on the same molecules but with different crystal structures, perhaps brought about by controlled cooling, may offer guidance on the role of local structure and the relevance of inter-molecular coupling, presumably via phonons. And of course, temperature plays an important role. When backed up by DFT calculations of the muoniated radical state and vibrational spectra for the radical, one may be able to bring all of the information together to perform modelling of the spin dynamics relevant to the muon, and possibly an alternative to the charge carrier motion models.

As has been indicated throughout the experimental section of this review, DFT calculations are essential to understand the localised muonium radical state that is present. They offer vital information on the HFCCs necessary to quantitatively analyse the data, as well as identify the particular adduct. This is essential information needed as input parameters for any modelling of the relaxation rate data, and may offer vital clues to the underlying relaxation mechanisms. However, we offer a word of caution; the theoretical approaches needed to accurately calculate the HFCCs of the muoniated radicals vary significantly between molecules. Indeed, prior to drawing conclusions from the calculations, one needs to benchmark the various methodologies for the specific molecule in question, as the the HFCCs are highly dependent on the specific combination of the basis set, functional and vibrational corrections for the molecule in question. Whilst this review has only considers the harmonic and anharmonic vibrations of relatively simple molecules (the acene series), these molecules do not display any rotational degrees of freedom that exist in a large number of organic molecules. In these simpler molecules, the agreement between experiment and theory is relatively good, but additional care is needed for the more complex molecules where bonds can rotate on axis. A good examples is the side groups in TIPS pentacene. Moreover, only the zero point energy corrections were taken into account in this review, but temperature will likely have a significant effect on the parameters extracted, and at finite temperature, these could cancel out any errors on the calculated HFCC that arise from the approximations involved in the functional or an inappropriate basis set.

Generally speaking, the performance of the basis sets is largely dependent on the size. In the molecules reviewed here, there is a considerable difference between the triple-ζ and double-ζ basis sets, although the triple-ζ basis set tend to perform nearly as well as the quadruple-ζ basis set, so it can be chosen if a compromise on computational time and accuracy is needed. However, this may not be true for all molecular systems and so care must be taken to benchmark. For systems where the triple-ζ basis set cannot be applied for geometry optimisation and/or averaging, the geometry can be firstly calculated by the double-ζ basis set or smaller, and an additional single point energy calculation with triple-ζ with can be done for the evaluation of isotropic HFCCs. Regarding the isotope effect of Mu, the anharmonic ZPE correction for the structure and isotropic HFCC of the muoniated radicals is more important than the harmonic ZPE correction, and can be undertaken by either Morse potential fit or V2PT method. They all produce reasonably good results, though the Morse potential fit approach is only correct for the HFCCs of muon. But since the V2PT method is much more computationally expensive, it is only recommended if the HFCCs of all the nuclei are of interest and the system is not too massive.

We conclude that if one does not benchmark, then agreement between experiment and theory can be the result of a cancellation of separate errors within the calculation. For example, too sharp a wave function at the muon's position, due to an artificially contracted s-orbital basis set, would result in an increase in the HFCC. An incorrect vibrationally averaged geometry, on the other hand, could result in a decrease of the HFCC. Another important effect is the functional itself. This can over-estimate the spin density distribution of the SOMO at the nuclear position and under estimate the spin polarisation of the DOMO, with the net result of a fortuitous cancellation of errors.

Similarly, could it be that there is a fortuitous superposition of signals in the experimental relaxation rates?

Alan Drew acknowledges financial support from the European Research Council ERC, project: MuSES. Leander Schulz and Sijie Zhang would like to acknowledge financial support from the National Science Foundation of China, grant numbers 61404088 and 61307039. Ke Wang would like to acknowledge financial support from the Chinese Scholarship Council.

1) P. Carretta, R. De Renzi, G. Prando and S. Sanna, Physica Scripta, **88**, 068504 (2013).
2) L. Nuccio, L. Schulz and A. J. Drew, J. Phys. D: Appl. Phys. **14**, 473001 (2014).
3) T. Lancaster, S. J. Blundell and F. L. Pratt, Physica Scripta **88**, 068506 (2013).
4) B. Patterson, Rev. Mod. Phys. **60**, 69 (1988).
5) S. F. J. Cox, R. L. Lichti, J. S. Lord, E. A. Davis, R. C. Vilao, J. M. Gil, T. D. Veal and Y. G. Celebi, Physica Scripta **88**, 068503 (2013).
6) M. Mansson and J. Sugiyama, Physica Scripta **88**, 068509 (2013).
7) N. J. Clayden, Physica Scripta **88**, 068507 (2013).
8) D Cammarerea, R.H Scheicher, N Sahoo, T.P Das and K Nagaminec, Physica B **289-290**, 636-639 (2000).
9) K. Nagamine, F. L. Pratt, S. Ohira, I. Watanabe, K. Ishida, S. N. Nakamura and T. Matsuzaki, Physica B **289** 631 (2000).
10) S. J. Blundell, Contemp. Phys. **40**, 175 (1999).
11) K. Nagamine, *Introductory Muon Science* (Cambridge University Press, 2007).
12) A. Schenck, *Muon Spin Rotation Spectroscopy: Principles and Applications in Solid State Physics* (Adam Hilger Ltd., 1985).
13) A. Yaouanc and P. Dalmas de Réotier *Muon Spin Rotation, Relaxation and Resonance* (Oxford Science Publications, 2011).
14) S. J. Blundell, Chem. Rev. **104**, 5717 (2004).
15) S. L. Lee, S. H. Kilcoyne, R. Cywinski, *Muon Science. Scottish Universities Summer School in Physics* (IOPP, Bristol, 1999).
16) R. H. Heffner and K. Nagamine, J. Phys.: Cond. Matt. **16**, Special issue on μSR (2004).
17) A. Amato, M. J. Graf, A. de Visser, H. Amitsuka, D. Andreica and A. Schenck, J. Phys.: Cond. Matt **16**, S4403 (2004).
18) R. Kadano, J. Phys.: Cond. Matt. **16**, S4421 (2004).
19) R. Khasanov, A. Shengelaya, E. Morenzoni, K. Conder, I. M. Savic and H. Keller, J. Phys.: Cond. Matt., **16** S4439 (2004).
20) H. Klauss, J. Phys.: Cond. Matt. **16**, S4457 (2004).
21) D. E. MacLaughlin, R. H. Heffner, O. O. Bernal, K. Ishida, J. E. Sonier, G. J. Nieuwenhuys, M. B. Maple and G. R. Stewart, J. Phys.: Cond. Matt. **16**, S4479 (2004).
22) J. E. Sonier, J. Phys.: Cond. Matt. **16**, S4499 (2004).
23) Y. J. Uemura, J. Phys.: Cond. Matt. **16**, S4515 (2004).
24) R. H. Heffner, D. E. MacLaughlin, G. J. Nieuwenhuys and J. E. Sonier, J. Phys.: Cond. Matt. **16**, S4541 (2004).
25) T. Lancaster, S. J. Blundell, F. L. Pratt, M. L. Brooks, J. L. Manson, E. K Brechin, C. Cadiou, C. Low, E. J. L. McInnes and R. E. P. Winpenny, J. Phys.: Cond. Matt. **16**, S4563 (2004).
26) E. Morenzoni, T. Prokscha, A. Suter, H. Luetkens and R. Khasanov, J. Phys.: Cond. Matt. **16**, S4583 (2004).
27) A. Keren, J. Phys.: Cond. Matt. **16**, S4603 (2004).
28) D. H. Ryan, J. van Lierop and J. M. Cadogan, J. Phys.: Cond. Matt. **16**, S4619 (2004).
29) A. Schenk and G. Solt, J. Phys.: Cond. Matt. **16**, S4639 (2004).
30) P. Dalmas de Réotier, P. C. M. Gubbens and A. Yaouanc, J. Phys.: Cond. Matt. **16**, S4687 (2004).
31) J. S. Lord, S. F. J. Cox, H. V. Alberto, J. Piroto Duarte and R. C. Vilao, J. Phys.: Cond. Matt. **16**, S4707 (2004).
32) R. L. Lichti, Y. G. Celebi, S. P. Cottrell, S. F. J. Cox and E. A. Davis, J. Phys.: Cond. Matt. **16**, S4721 (2004).
33) J. S. Lord, S. F. J. Cox, M. Charlton, D. P. Van der Werf, R. L. Lichti and A. Amato, J. Phys.: Cond. Matt. **16**, S4739 (2004).
34) V. G. Storchak, D. G. Eshchenko and J. H. Brewer, J. Phys.: Cond. Matt. **16**, S4761 (2004).
35) F. L. Pratt J. Phys.: Cond. Matt. **16**, S4779 (2004).
36) K. Nagamine and E. Torikai, J. Phys.: Cond. Matt. **16**, S4797 (2004).
37) S. Cottrell, Physica Scripta, 88, 068501 (2013).
38) P. J. C. King, R. de Renzi, S. P. Cottrell, A. D. Hillier and S. F. J. Cox, Physica Scripta **88**, 068502 (2013).
39) D. T. Adroja, A. D. Hillier, Y. Muro, T. Takabatake, A. M. Strydom, A. Bhattacharyya, A. Daoud-Aladin and J. W. Taylor, Physica Scripta, **88**, 068505 (2013).
40) M. Ricco, M. Aramini, M. Mazzani, D. Pontiroli, M. Gaboardi and O. V. Yazyev, Physica Scripta **88**, 068508 (2013).
41) J. S. Moller, P. Bonfa, D. Ceresoli, F. Bernardini, S. J. Blundell, T. Lancaster, R. De Renzi, N. Marzari, I. Watanabe, S. Sulaiman, S. Sulaiman and M. I. Mohamed-Ibrahimfull, Physica Scripta **88**, 068510 (2013).
42) K. Yokoyama, P. Murahari, P. Heathcote, L. Nuccio, J. S. Lord, N. A. Morley and A. J. Drew, Physica Scripta **88**, 068511 (2013)
43) D. N. Sathayanarayana *Introduction to Magnetic Resonance Spectroscopy ESR, NMR, NQR* (IK International Publishing House, 2009).
44) D. C. Walker, Radiat. Phys. Chem. **47**, 23 (1996).
45) A. Mozumder (Eds.: M. Burton. and J. L. Magee), *Advances in Radiation Chemistry Vol. I* (Wiley-Interscience, New York, 1969).
46) P. J. Cormier, C. Alcorn, G. Legate and K. Ghandi, Radiation Research **181**, 396 (2014).
47) K. Ghandi, I. P. Clark, J. S. Lord and S. P. Cottrell, Phys. Chem. Chem. Phys. **9**, 353 (2007).
48) I. D. Reid, D. M. Garner, I. Y Lee, M. Senba, D. J. Arsenau and D. G. Fleming, J. Chem. Phys. **86**, 5578 (1987).
49) K. Ghandi, B. Addison-Jones, J.-C. Brodovitch, I. McKenzie, P.W Percival and J. Schuth, Phys. Chem. Chem. Phys. **4** 586, (2002).
50) E. Roduner Chem. Soc. Rev. **29**, 337 (1993). U. C. Dawin, H. Dilger, E. Roduner, R. Scheuermann, A. Stoykov, G. Giesselmann, Angew. Chem. Int. Ed. **49**, 2427 (2010).
51) K. Ghandi and Am MacLean, Hyp. Int.
52) S. F. J. Cox, Sol. State Nucl. Mag. Res. **11**, 102 (1998)
53) E. Roduner, M. Stolmar, H. Dilger and I. D. Reid, J. Phys. Chem. A **102**, 7591 (1998).
54) J. S. Lord, Physica B **374**, 472 (2006)
55) S. R. Kreitzman and E. Roduner, Chem. Phys. **192**,189 (1995).
56) I. D. Reid, T. Azuma and E. Roduner, Nature **345**, 328 (1990)
57) L. Schulz, M. Willis, L. Nuccio, P. Shusharov, S. Fratini, F. L. Pratt, W. P. Gillin, T. Kreouzis, M. Heeney, N. Stingelin, C. A. Stafford, D. J. Beesley, C. Bernhard, J. E. Anthony, I. McKenzie, J. S. Lord, and A. J. Drew, Phys. Rev. B, **84** 085209 (2011).
58) R. F. Kiefl, J. W. Schneider, A. MacFarlane, K. Chow, T. L. Duty, T. L. Estle, B. Hitti, R. L. Lichti, E. J. Ansaldo, C. Schwab, P. W. Percival, G. Wei, S. Wlodek, K. Kojima, W. J. Romanow, J. P. McCauley, Jr., N. Coustel, J. E. Fischer, and A. B. Smith, Phys. Rev. Lett. **68**, 2708 (1992)
59) L Nuccio, L Schulz, M Willis, F L Pratt, M Heeney, N Stingelin, C Bernhard and A J Drew, J. Phys.: Conf. Ser. **292**, 012004 (2011).
60) L. Nuccio, M. Willis, L. Schulz, S. Fratini, F. Messina, M. D?Amico, F. L. Pratt, J. S. Lord, I. McKenzie, M. Loth, B. Purushothaman, J. Anthony, M. Heeney, R. M. Wilson, I. Hernandez, M. Cannas, K. Sedlak, T. Kreouzis, W. P. Gillin, C. Bernhard, and A. J. Drew, Phys. Rev. Lett. **110**, 216602 (2013).
61) S. Han, K. Wang, M. Willis, L. Nuccio, F.L. Pratt, J.S. Lord, K.J. Thorley, J. Anthony, A.J. Drew, S. Zhang, L. Schulz, Synthetic Metals **208** 39 (2015).
62) P. F. Meier Phys. Rev. A **25**, 1287 (1982).
63) M. Heming, E. Roduner ans B. D. Patterson Hyp. Int. **32** 727 (1986).
64) F. Devreux, J. P. Boucher and M. Nechtschein J. Physique **35** 19 (1974).
65) M. A. Butler, L. R. Walker and Z. G. Soos J. Chem. Phys. **64** 3592 (1976).
66) K. Mizoguchi Makromol. Chem. Makromol. Symp. **37** 53 (1990).
67) K. Mizoguchi and K. Kume Sol. Stat. Commun. **89** 971 (1993).
68) R. Risch and K. W. Kehr Phys. Rev. B **46** 5246 (1992).
69) http://www.psi.ch
70) E. Morenzoni, E.M. Forgan, H. Gluckler, T.J. Jackson, H. Luetkens, C. Niedermayer, T. Prokscha, T.M. Riseman, M. Birke, A. Hofer, J. Litterst, M. Pleines and G. Schatz, Hyp. Int. **133** 179 (2001).
71) E. Morenzoni, H. Gluckler, T. Prokscha, R. Khasanov, H. Luetkens, M. Birke, E. M. Forgan, Ch. Niedermayer and M. Pleines, Nucl. Inst. Meth. B **192** 254 (2002).
72) E. Morenzoni, F. Kottmann, D. Maden, B. Matthias, M. Meyberg, Th. Prokscha, Th. Wutzke, and U. Zimmermann Phys. Rev. Lett. **72(17)** 2793 (1994).
73) K. Nagamine, K. Ishida, T. Matsuzaki, K. Nishiyama, Y. Kuno, T. Yamazaki, and H. Shirakawa, Phys. Rev. Lett. **53** 1763 (1984).

74) K. Ishida, K. Nagamine, T. Matsuzaki, Y. Kuno, T. Yamazaki, E. Torikai, H. Shirakawa, and J. H. Brewer, Phys. Rev. Lett., **55** 2009 (1985).
75) K. Nagamine, K. Ishida Hyp. Int. **32** 535 (1986).
76) F. L. Pratt, S. J. Blundell, Th. Jestadt, B. W. Lovett, A. Husmann, I. M. Marshall, W. Hayes, A. Monkman, I. Watanabe, K. Nagamine, R. E. Martin and A. B. Holmes, Physica B, **289** 625 (2000).
77) F. L. Pratt, S. J. Blundell, W. Hayes, K. Nagamine, K. Ishida, and A. P. Monkman Phys. Rev. Lett. **79** 2855 (1997).
78) S. J. Blundell, F. L. Pratt, I. M. Marshall, C. A. Steer, W. Hayes, A. Husmann, C. Fischmeister, R. E. Martin and A. B. Holmes, J. Phys.: Cond. Mat. **14** 9987 (2002).
79) F.L. Pratt, W. Hayes, G.R. Mitchell, B. Rossi, M.S. Kiani, B.D. Malhotra, S.S. Pandey, A. Miltond and A.P. Monkman, Synth. Met. **55** 677 (1993).
80) F. L. Pratt, G. R. Mitchell, S. F. J. Cox, C. A. Scott and W. Hayes, Hyp. Int. **65** 847 (1990).
81) F.L. Pratt, K. Ishida, K. Nagamine, P.A. Pattenden, Th. Jestadt, K.H. Chow, S.J. Blundell, W. Hayes and A.P. Monkman, Synth. Met. **84** 943 (1997).
82) F.L. Pratt, K. Ishida, K. Nagamine, P.A. Pattenden, Th. Jestadt, K.H. Chow, S.J. Blundell, W. Hayes and A.P. Monkman, Hyp. Int. **106** 33 (1997).
83) F.L. Pratt, S.J. Blundell, B.W. Lovett, K. Nagamine, K. Ishida, W. Hayes, Th. Jestadt and A.P. Monkman, Synth. Met. **101** 323 (1999).
84) F.L. Pratt, R.M. Valladares, P.A. Pattenden, S.J. Blundell, W. Hayes, A.P. Monkman and K. Nagamine, Synth. Met. **69** 231 (1995).
85) N. A. Morley, private communication.
86) F. L. Pratt J. Phys.: Cond. Mat. **16** S4779 (2004).
87) K. Nagamine, Eur. Phys. J. A **13** 189 (2002).
88) R.H. Scheicher, D. Cammarere, N. Sahoo, T.M. Briere, F.L. Pratt, K. Nagamine and T.P. Das Physica. B **326** 30 (2003).
89) M. T. F. Telling and S. H. Kilcoyne, Phys. Proc. **30** 86 (2012).
90) M. T. F. Telling and S. H. Kilcoyne, J. Phys.: Cond. Mat. **19** 026221 (2007).
91) E. Torikai, K. Nagamine, F. L. Pratt, I. Watanabe, Y. Ikedo, H. Urabe and H. Grimm Hyp. Int. **138** 509 (2001).
92) K. Nagamine and E. Torikai J. Phys.: Cond. Mat. **16** S4797 (2004).
93) R.H. Scheicher, T.P. Das, E. Torikai, F.L. Pratt and K. Nagamine, Physica B **374** 448 (2006).
94) K. Nagamine, K. Shimomura, K. Imai and J. S. Schultz, Physica B **374** 444 (2006).
95) J. P. Duarte, R.C. Vilao, J.M. Gil, H.V. Alberto, N. Ayres de Campos and A. Weidinger, Physica B **326** 94 (2003).
96) J. P. Duarte, R. C. Vilao, H. V. Alberto, J. M. Gil, F. P. S. C. Gil, A. Weidinger, N. Ayres de Campos and K. Fostiropoulos, Phys. Rev. B **73**, 075209 (2006).
97) J. P. Duarte, H. V. Alberto, R. C. Vilao, J. M. Gil, A. Weidinger and N. Ayres de Campos Phys. Stat. Sol. C **7** 996 (2010).
98) J. P. Duarte, R.C. Vilao, H.V. Alberto, J.M. Gil and N. Ayres de Campos, Physica B **404** 859 (2009).
99) A. J. Drew, F. L. Pratt, J. Hoppler, L. Schulz, V. Malik-Kumar, N. A. Morley, P. Desai, P. Shakya, T. Kreouzis, W. P. Gillin, K. W. Kim, A. Dubroka, and R. Scheuermann, Phys. Rev. Lett. **100** 116601 (2008).
100) T. P.I. Saragi, Risdiana, L. Safriani, I. Kawasaki, J. Salbeck, I. Watanabe, Org. Elec. **14** 62 (2013).
101) I McKenzie, J. Phys. Chem. A **114** 12759 (2010).
102) L. Schulz, K. Wang, M. Willis, L. Nuccio, P. Murahari, S. Zhang, F. L. Pratt, J. S. Lord, N. A. Morley, C. Bernhard and A. J. Drew, J. Phys.: Conf. Ser. **551** 012042 (2014).
103) M. Heming, E. Roduner, I. D. Reid, P. W. F. Louwrier, J. W. Schneider, H. Keller, W. Odermatt, P. D. Patterson, H. Simmler, B. Pumpin, I. M. Savic (1989).
104) S. Pramanik, C. G. Stefanita, S. Patibandla, S. Bandyopadhyay, K. Garre, N. Harth and M. Cahay, Nat. Nano. **2** 216 (2007).
105) P. Shakya, P. Desai, M. Somerton, G. Gannaway, T. Kreouzis and W. P. Gillin J. Appl. Phys. **103**, 103715 (2008).
106) V. Alek Dediu, Luis e. Hueso, Ilaria Bergenti and Carlo Taliani, Nature Materials **8** 707 (2009).
107) A. J. Drew, J. Hoppler, L. Schulz, F. L. Pratt, P. Desai, P. Shakya, T. Kreouzis, W. P. Gillin, A. Suter, N. A. Morley, V. K. Malik, A. Dubroka, K. W. Kim, H. Bouyanfif, F. Bourqui, C. Bernhard, R. Scheuermann, G. J. Nieuwenhuys, T. Prokscha and E. Morenzoni, Nat. Mat., **8** 109 (2009).
108) L. Schulz, L. Nuccio, M. Willis, P. Desai, P. Shakya, T. Kreouzis, V. K. Malik, C. Bernhard, F. L. Pratt, N. A. Morley, A. Suter, G. J. Nieuwenhuys, T. Prokscha, E. Morenzoni, W. P. Gillin and A. J. Drew, Nat. Mat., **10** 39 (2011).
109) http://www.srim.org
110) S. R. Forrest, Nature **428** 911 (2004).
111) F. J. Wang and Z. V. Vardeny, Synth. Met. **160** 210 (2010).
112) F. J. Wang, C. G. Yang, Z. V. Vardeny and X. G. Li, Phys. Rev, B **75** 245324 (2007).
113) W. R. Salaneck, K. Seki, A. Kahn, J. J. Pireaux, *Conjugated Polymer and Molecular Interfaces* (Marcel Dekker, 2002).
114) H. Ishii, K. Sugiyama, E. Ito and K. Seki, Adv. Mat. **11** 605 (1999).
115) A. Hofmann, Z. Salman, M. Mannini, A. Amato, L. Malavolti, E. Morenzoni, T. Prokscha, R. Sessoli, and A. Suter ACS Nano **6** 8390 (2012).
116) A Hofmann and Z Salman, J. Phys. Conf. Series **551** 012055 (2014).
117) H. Sekino and R. J. Bartlett, J. Chem. Phys. **82**, 4225 (1985).
118) W. Kohn, Int. J. Quantum Chem., Quantum Chem. Symp. **56**, 4 (1995).
119) L. A. Eriksson, V. G. Malkin, O. L. Malkin and D. R. Salahub, J. Chem. Phys. **99**, 9756 (1993).
120) L. A. Eriksson, V. G. Malkin, O. L. Malkin and D. R. Salahub, Int. J. Quant. Chem. **52**, 879 (1994).
121) N. Ishii and T. Shimizu, Chem. Phys. Let. **225**, 462 (1994).
122) M. Kaupp, M. Bhl and V. G. Malkin, *Calculation of NMR and EPR Parameters: Theory and Applications* (WILEY-VCH Verlag GmbH & Co. KGaA , 2004).
123) V. Barone et al., *in Recent Advances in Density Functional Methods, Part 1*, ed. D. P. Chong (World Scientific Publ. Co., Singapore, 1996) p. 287-334.
124) S. Fau and R. J. Bartlett, J. Phys. Chem. A **107**, 6648 (2003).
125) J. Hiller, J. Sucher, and G. Feinberg, Phys. Rev. A **18**, 2399 (1978).
126) J. E. Harriman, Int. J. Quant. Chem. **17**, 689 (1980).
127) M. Challacombe and J. Cioslowski, J. Chern. Phys. **100**, 464 (1994).
128) V. A. Rassolov and D. M. Chipman, J. Chern. Phys. **105**, 1470 (1996).
129) V. A. Rassolov and D. M. Chipman, J. Chern. Phys. **105**, 1479 (1996).
130) L. Liang and V. A. Rassolov, J. Phys. Chem. C **114**, 20648 (2010).
131) A. J. Cohen, P. Mori-Snchez and W. Yang, Science **321**, 792 (2008).
132) P. W. Percival, R. F. Kiefl, S. R. Kreitzman, D. M. Garner, S. F.J. Cox, G. M. Luke, J. H. Brewer, K. Nishiyama, K. Venkateswaran, Chem. Phys. Let., **133**, 465 (1987).
133) J. J. P. Stewart, J. Comput. Chem. **10**, 209 (1989).
134) J. He, J. Du, T. Kreouzis, F. L. Pratt, J. S. Lord, M. T.F. Telling, A. J. Drew, N. A. Morley and M. Willis, Syn. Met. **208**, 21 (2015).
135) O. Hammerich, M. F. Nielsen,H. Zuilhof, P. P. J. Mulder, G. Lodder, R. C. Reiter, D. E. Kage, C. V. Rice and C. D. Stevenson, J. Phys. Chem., **100**, 3454 (1996).
136) H. Zuilbof and G. Ladder, J. Phys. Chem. **96**, 6957 (1992).
137) N. O. *İ*skeleli, H. Karabıyık, Ç. Albayrak, H. Petek and E. Ağar, Struct. Chem. **17**, 393 (2006).
138) P. J. Stang, C. M. Crittell, A. M. Arif, M. Karni, and Y. Apeloig, J. Am. Chem. SOC. **113**, 7461 (1991).
139) U. C. Abdul Jaleel, M. Rakhila, and G. Parameswaran, Advan. Phys. Chem. **2010** 787813 (2010).
140) W. Fujita and K. Awagal, Science **286**, 261 (1999).
141) W. Fujita, K. Awaga, H. Matsuzaki and H. Okamoto, Phys. Rev. B **65**, 064434 (2002).
142) I. McKenzie, J. Phys. Chem. A **114**, 1275 (2010).
143) E. Roduner and I.D. Reid, Isr. J. Chem. **29**, 3 (1989).
144) A.L de Magalhaẽs and M. J. Ramos, Chem. Phys. Lett. **165**, 528 (1990).
145) M. I. J. Probert and A. J. Fisher, Chem. Phys. L. **259**, 271 (1996).
146) B. S. Hudson and S. K. Chafetz, Molecules **18**, 4906 (2013).
147) M. Kaupp, M. Bhl and V. G. Malkin, *Calculation of NMR and EPR Parameters: Theory and Applications* (WILEY-VCH Verlag GmbH & Co. KGaA , 2004) p. 201-205.
148) M. Straka, M. Kaupp and E. l. Roduner, Theor. Chem. Acc. **114**, 318 (2005).
149) I. McKenzie, J. C. Brodovitch, K. Ghandi, S. Kecman and P.W. Percival, Phys. B **326**, 76 (2003).
150) M. I. J. Probert and A. J. Fisher, J.Phys.: Con. Mat. **9**, 3241 (1997).
151) R. M. Macrae and I. Carmichael, J. Phys. Chem. A **105**, 3641 (2001).
152) Y. K. Chen, D. G. Fleming, and Y. Alexander Wang, J. Phys. Chem. A **115**, 2765 (2011).
153) V. Filidou, D. Ceresoli, J. J. L. Morton, and F. Giustino, Phys. Rev. B **85**, 115430 (2012).
154) M. Buncher, Eur. J. Phys. **21**,19 (2000).

155) S. A. Perera, J. D. Watts and R. J. Bartlett, J. Chem. Phys. **100**, 1425 (1994).
156) F. Pratt, Phil. Mag. Lett. **75**, 371 (1997).
157) S. F. Boys, Proc. R. Soc. London Ser. A **200**, 542 (1950).
158) T. Kato, Commu. on Pure and Appl. Math. **10**, 151 (1957).
159) W. Meyer, J. Chem. Phys. **51**, 5149 (1969).
160) S. L. Thomas and I. Carmichael, Phys. B **374-375**, 290 (2006).
161) T. H. Dunning Jr., J. Chem. Phys. **90**, 1007 (1989).
162) D. E. Woon and T. H. Dunning Jr., J. Chem. Phys. **98**, 1358 (1993).
163) N. Godbout, D. R. Salahub, J. Andzelm and E. Wimmer, Can. J. Chem. **70**, 560 (1992).
164) P. Hohenberg and W. Kohn, Phys. Rev. **136**, B864 (1964).
165) W. Kohn and L. J. Sham, Phys. Rev. **140**, A1133 (1965).
166) J. P. Perdew, A. Ruzsinszky, J. Tao, V. N. Staroverov, G. E. Scuseria and G. I. Csonka, J. Chem. Phys. **123**, 062201 (2005).
167) A. D. Becke, Phys. Rev. A **38**, 3098 (1988).
168) J. P. Perdew, J. A. Chevary, S. H. Vosko, Koblar A. Jackson, Mark R. Pederson, D. J. Singh, and Carlos Fiolhais, Phys. Rev. B **46**, 6671 (1992).
169) J. P. Perdew, K. Burke and M. Ernzerhof, Phys. Rev. Lett. **77**, 3865 (1996).
170) C. Lee, W. Yang, and R. G. Parr, Phys. Rev. B **37**, 785 (1988).
171) S. H. Vosko, L. Wilk, and M. Nusair, Can. J. Phys. **58**, 1200 (1980).
172) A. D. Becke, Phys. Rev. B **37**, 785 (1988).
173) J. P. Perdew, M. Ernzerhof and K. Burke, J. Chem. Phys. **105**, 9982 (1996).
174) E. Engel and Reiner M. Dreizler *Density Functional Theory: An Advanced Course* (Sprintger-Veleg Berlin Heidelberg 2011).
175) O. A. Vydrov and G. E. Scuseria, J. Chem. Phys. **125**, 234109 (2006).
176) T. Yanai, D. P Tew and N.C Handy, Chem. Phys. Lett. **393**, 51 (2004).
177) J. -D. Chai and M. Head-Gordon, Phys. Chem. Chem. Phys. **10**, 6615 (2008)
178) R. W. Fessenden, J. Phys. Chem. **71**, 74 (1967).
179) E. B. Wilson JR., J. C. Decius and P. C. Cross, *Molecular Vibrations: The Theory of Infrared and Raman Vibrational Spectra* (McGraw-Hill Book Company, 1955) p. 11-48.
180) McQuarrie, A. (2000) Statistical Mechanics, University Science Books, California.
181) D. C. Walker, J. Phys. Chem. **85**, 3960 (1981).
182) D. C. Walker *Muon and Muonium Chemistry* (Press Syndicate of the University of Cambridge, 1983).
183) M. I. Millis, J. Mol. Spec. **5**, 334 (1961).
184) Gaussian 09, Revision C.01, M. J. Frisch, G. W. Trucks, H. B. Schlegel, G. E. Scuseria, M. A. Robb, J. R. Cheeseman, G. Scalmani, V. Barone, B. Mennucci, G. A. Petersson, H. Nakatsuji, M. Caricato, X. Li, H. P. Hratchian, A. F. Izmaylov, J. Bloino, G. Zheng, J. L. Sonnenberg, M. Hada, M. Ehara, K. Toyota, R. Fukuda, J. Hasegawa, M. Ishida, T. Nakajima, Y. Honda, O. Kitao, H. Nakai, T. Vreven, J. A. Montgomery, Jr., J. E. Peralta, F. Ogliaro, M. Bearpark, J. J. Heyd, E. Brothers, K. N. Kudin, V. N. Staroverov, T. Keith, R. Kobayashi, J. Normand, K. Raghavachari, A. Rendell, J. C. Burant, S. S. Iyengar, J. Tomasi, M. Cossi, N. Rega, J. M. Millam, M. Klene, J. E. Knox, J. B. Cross, V. Bakken, C. Adamo, J. Jaramillo, R. Gomperts, R. E. Stratmann, O. Yazyev, A. J. Austin, R. Cammi, C. Pomelli, J. W. Ochterski, R. L. Martin, K. Morokuma, V. G. Zakrzewski, G. A. Voth, P. Salvador, J. J. Dannenberg, S. Dapprich, A. D. Daniels, O. Farkas, J. B. Foresman, J. V. Ortiz, J. Cioslowski, and D. J. Fox, Gaussian, Inc., Wallingford CT, 2010.
185) K. Eiben and R. H. Schuler, J. Chem. Phys. **62**, 3093 (1975).
186) I. D. Reid and E. Roduner, Struct. Chem. **2**, 419 (1990).
187) Paul W. Percival, B. Addison-Jones, J. Brodovitch, K. Ghandi, and J. Schüth, Can. J. Chem. **77**, 326 (1999).
188) Data from TF-μSR measurement at PSI in November 2014.
189) Data extracted from TF-μSR measurement at PSI in November 2014 and ALC-μSR measurement at ISIS in December 2013.